Single-pulse Transcranial Magnetic Stimulation Affects Working-memory Performance via Posterior Beta-band Oscillations

Jacqueline M. Fulvio[1], Saskia Haegens[2,3,4], and Bradley R. Postle[1]

Abstract

■ A single pulse of TMS (spTMS) during the delay period of a double serial retrocuing working-memory task can briefly rescue decodability of an unprioritized memory item (UMI). This physiological phenomenon, which is paralleled in behavior by involuntary retrieval of the UMI, is carried by the beta frequency band, implicating beta-band dynamics in priority coding in working memory. We decomposed EEG data from 12 participants performing double serial retrocuing with concurrent delivery of spTMS using Spatially distributed PhAse Coupling Extraction. This procedure decomposes the scalp-level signal into a set of discrete coupled oscillators, each with a component strength that can vary over time. The decomposition revealed a diversity of low-frequency components, a subset of them strengthening with the onset of the task, and the majority declining in strength across the trial, as well as within each delay period. Results with spTMS revealed no evidence that it works by activating previously "silent" sources; instead, it had the effect of modulating ongoing activity, specifically by exaggerating the within-delay decrease in strength of posterior beta components. Furthermore, the magnitude of the effect of spTMS on the loading strength of a posterior beta component correlated with the disruptive effect of spTMS on performance, a pattern also seen when analyses were restricted to trials with "UMI-lure" memory probes. Rather than reflecting the "activation" of a putatively "activity silent" UMI, these results implicate beta-band dynamics in a mechanism that distinguishes prioritized from unprioritized, and suggest that the effect of spTMS is to disrupt this code. ■

INTRODUCTION

TMS works on the principle that when a brief (< 1 msec) magnetic pulse is passed through the scalp, a current is induced in the brain tissue experiencing this pulse (e.g., Walsh & Rushworth, 1999). The experimental procedure of applying a single pulse of TMS (spTMS) while concurrently recording the EEG has provided many important insights about human neurophysiology and about links between neurophysiology and behavior. For example, when spTMS is delivered over occipital versus parietal versus frontal cortex, the resultant spectral perturbations are most prominent at 8 Hz, 19 Hz, and 29 Hz, respectively, suggesting different natural frequencies for the corticothalamic circuitry in these three regions (Rosanova et al., 2009). Although these results were derived when participants were at rest, their functional relevance is demonstrated, for example, when spTMS is delivered to induce the visual perception of a phosphene. When occipital cortex is targeted, phosphene induction is dependent on pre-spTMS power and phase in the alpha band of the EEG (e.g., Samaha, Gosseries, & Postle, 2017; Romei et al., 2008), and when parietal cortex is targeted, phosphene induction is dependent on pre-spTMS power in the low beta band (12–22 Hz; Samaha et al., 2017). These results suggest that oscillations at these frequencies reflect fluctuations of cortical excitability and/or of temporal windows for the routing of signals.

spTMS phosphene induction results also highlight a question about the physiological bases of the spTMS spectral perturbation (e.g., Rosanova et al., 2009). One possibility is that this response results from the triggering (or driving) of a new source of activity in the brain—that is, that one or more circuits that were previously inactive become "activated" by the pulse of induced current. Alternatively, a second possibility is hinted at by a further comparison of spTMS phosphene induction resulting from occipital versus parietal stimulation: Despite the dependence of these two protocols on the state of distinct frequency bands pre-spTMS, the poststimulus correlates of phosphene perception were highly similar across the two (Samaha et al., 2017). This is consistent with the idea that functionally effective spTMS may arise from the modulation of ongoing activity (e.g., because of phase reset and/or modulations of the amplitude of endogenous oscillations).

Adjudicating between "activation" versus "modulation" accounts of evoked responses measured at the scalp is notoriously difficult, due in part to the fact that the signal recorded at each electrode is a blend of signals from

[1]University of Wisconsin–Madison, [2]Columbia University, [3]New York State Psychiatric Institute, [4]Radboud University Nijmegen

multiple underlying sources. And because there is always oscillatory power in the signal preceding the delivery of the pulse, one cannot know the extent to which spTMS-related changes in sensor-level activity are because of the "activation" of previously silent sources (and/or to the "deactivation" of previously active sources) versus to the modulation of the power and/or phase of ongoing sources of activity. In this report, we sought to overcome this challenge by transforming an EEG data set with a decomposition procedure that extracts patterns of activity that are more informative of the underlying sources. The procedure is called Spatially distributed PhAse Coupling Extraction (SPACE). Conceptually, SPACE is an extension of parallel-factor analysis that relies on a plausible model of a neurobiological rhythm: a spatially distributed oscillation with energy in a range of frequencies, and involving between-sensors phase relations that can vary over frequencies (van Der Meij, van Ede, & Maris, 2016). The result is a set of topographically overlapping components separated by their patterns of between-sensors phase coupling, their spectral content, and their variable presence over trials. In other words, SPACE effects a decomposition of the EEG signal measured at the scalp into components comprising discrete coupled oscillators that can be construed as arising from discrete sources. When applied to an spTMS data set, we reasoned that an "activation" mechanism of the spTMS spectral perturbation would manifest as the appearance/disappearance of components time-locked to the delivery of spTMS. Absence of evidence for spTMS-related appearance/disappearance of components, in contrast, would be more consistent with a "modulation" account.

The data set to which we applied the SPACE decomposition was collected while participants performed a double serial retrocuing (DSR) working memory (WM) task (Fulvio & Postle, 2020). We chose this data set because the "activation" versus "modulation" accounts of the mechanisms of spTMS have theoretical implications for the interpretation of a functional effect of spTMS delivered during the DSR task. In this task, two items are presented as samples and then one of the two is cued as the one that will be tested by the impending recognition probe (i.e., a "retrocue"). Importantly, the uncued item assumes the status of a "unprioritized memory item" (UMI) that is irrelevant for, and therefore should not influence, the assessment of the impending memory probe. A key finding from this task is that, on trials when the UMI is presented as the recognition probe—that is, as a "lure" that participants should reject as a nonmatch–spTMS delivered before these lure probes selectively increases the likelihood that participants will (incorrectly) endorse them. That is, spTMS increases the likelihood that the UMI will intrude on the recognition decision (Fulvio & Postle, 2020; Rose et al., 2016). Thus, by analogy to how spTMS to occipital or parietal cortex can trigger the perception of a phosphene, spTMS delivered during the delay period of a WM task can be construed as triggering the involuntary retrieval of unprioritized information being held in WM. The way that it does so has important implications for how this unprioritized information had been represented. In particular, did spTMS activate the UMI from an "activity-silent" state (Rose et al., 2016; cf. Stokes, 2015; Barak & Tsodyks, 2014), or did spTMS modulate an ongoing oscillatory state that had kept it in an active, but "action-null," functional state (cf. Wan, Ardalan, Fulvio, & Postle, 2024; Wan, Menendez, & Postle, 2022; Wan, Cai, Samaha, & Postle, 2020; Yu, Teng, & Postle, 2020)?

The phenomenon of the spTMS-triggered "involuntary retrieval" of the UMI has been studied previously with EEG (Rose et al., 2016).[1] At the beginning of the trial, an active representation of both stimuli could be decoded with multivariate pattern analysis applied to the broadband EEG signal, and this decoding was also successful when restricted to bandpass-filtered signal from the alpha band (Rose et al., 2016). Then, following the first cue, decodability of the uncued item declined to baseline levels, a pattern that parallels its transition to the functional status of UMI.[2] When spTMS was delivered after this loss of decodability (and before probe onset), however, the decodability of the UMI was transiently recovered. Furthermore, this recovery of decodability was isolated to signal in the beta band (Rose et al., 2016). In addition to this specific evidence for a possible role for beta-band oscillatory dynamics in the spTMS-triggered "involuntary retrieval" from WM, there is a growing body of literature establishing, more generally, an important role for beta-band activity in other aspects of working memory function (ElShafei, Zhou, & Haegens, 2022; Proskovec, Wiesman, Heinrichs-Graham, & Wilson, 2019; Haegens, Vergara, Rossi-Pool, Lemus, & Romo, 2017; von Lautz et al., 2017; Siegel, Warden, & Miller, 2009; Axmacher, Schmitz, Wagner, Elger, & Fell, 2008; Deiber et al., 2007; Tallon-Baudry, Bertrand, Peronnet, & Pernier, 1998). Consequently, SPACE-identified components in the beta band were a focus of the work reported here.

To summarize, for the current report, we first carried out a neurobiologically informed decomposition of EEG data collected from participants performing the DSR WM task and then carried out three sets of hypothesis-testing analyses. The first addressed the general question of whether the spTMS-related spectral perturbation of the EEG is better understood as a consequence of an "activation" or a "modulation" mechanism. The second exploited the method's ability to quantify individual component strengths at varying points in time to characterize the task-related and spTMS-related dynamics of low-frequency components of the EEG during the DSR task. The third assessed the consequences for behavior of the effects of spTMS on these low-frequency components. The results from these analyses emphasize an important role for oscillatory dynamics in the beta band and illustrate ways in which a neurally informed, data-driven decomposition of EEG data can yield novel insights that could not be obtained from analyses of untransformed data.

METHODS

Behavioral results from this experiment have been reported previously (Fulvio & Postle, 2020).

Participants

Fourteen neurologically healthy members of the University of Wisconsin–Madison community, with no reported contraindications for magnetic resonance imaging (MRI) or TMS, were recruited for the study. The target sample size was 12, a number chosen according to an a priori power analysis based on the behavioral results of Experiment 4 of Rose and colleagues (2016) that indicated that 12 participants would be needed to achieve 80% power in the critical behavioral comparison of interest (see Fulvio & Postle, 2020).[3] Each of the 14 participants underwent a structural MRI scan and participated in three sessions of WM task performance with concurrent EEG and spTMS, each on separate days. Data from two individuals were excluded because of noncompliance with task instructions during the behavioral sessions resulting in a final sample size of 12 participants (five female participants) with age range of 18–28 years (M = 21.7 years), all right-handed. All participants had normal or corrected-to-normal vision with contact lenses (eyeglasses were not compatible with the TMS targeting apparatus), and all reported having normal color vision. The research complied with the guidelines of the University of Wisconsin–Madison's Health Sciences Institutional Review Board. All participants gave written informed consent at the start of each session and received monetary compensation in exchange for participation.

Experimental Procedure

The experiment took place over four separate sessions. The first session involved an MRI scan, which acquired the anatomical image used to guide spTMS during the three behavioral sessions. During each behavioral session, participants performed two WM tasks, a DSR task and a single retrocue task. (For the current study, we analyzed data collected during the DSR task only.) The tasks were carried out in alternating blocks, with each of the three sessions comprising eight 30-trial blocks. The order of the blocks was switched across sessions within participants and counterbalanced across participants.

Double-serial Retrocue Task

The DSR task (Figure 1A) began with the simultaneous presentation of two sample items, one drawn from each of two of three categories (faces, words, and dot motion—see Fulvio and Postle [2020] for more details about the stimuli), with one item presented above central fixation and one item below (2 sec), followed by 5 sec of fixation (*Delay 1.1*), followed by a 500-msec cue (*Cue 1*; dotted line) whose location (i.e., above or below fixation) indicated which of the two samples would be tested, followed by 4.5 sec of fixation (*Delay 1.2*), followed by a recognition probe (1 sec) and response period (1 sec). Then, the trial continued with a second 500-msec cue (*Cue 2*) followed by *Delay 2* (4.5 sec) and *Probe 2* (1 sec, plus an additional 1-sec response capture window). Cue 2 appeared in the same location as Cue 1 on 50% of trials. The intertrial interval was 2 sec.

Participants indicated a "match" or "nonmatch" judgment as to whether the probe stimulus was a match to the cued memory item by keyboard button press. Fifty percent of probe stimuli were matches of the cued item, 30% were nonmatches drawn from the same stimulus category as the cued item, and 20% were the uncued item from that trial's memory set (i.e., lures). Participants were not explicitly told that the uncued memory item could appear as lures; nevertheless, lures were scored as "nonmatches." When the response was registered, feedback was provided—the fixation cross turned green for correct responses, red for incorrect responses—for the remainder of the response window. Throughout each block, the TMS coil was positioned to target area IPS2 in the right hemisphere, and spTMS was delivered (unpredictably) as follows: On and 25% of trials, spTMS was delivered during both delay periods, on 25% of trials, spTMS was delivered only during the first delay period, on 25%, spTMS was delivered only during the second delay period, and on 25% of trials, spTMS was not delivered. Order of memory set, cued category, and probe type were randomized, with the constraint that spTMS was delivered on 50% of trials of each type.

MRI Acquisition and Preprocessing

Whole-brain images were acquired with a 3 T MRI scanner (Discovery MR750; GE Healthcare) at the Lane Neuroimaging Laboratory at the University of Wisconsin–Madison. High-resolution, T1-weighted images were acquired for all participants with a fast spoiled gradient-echo sequence (8.2-msec repetition time, 3.2-msec echo time, 12° flip angle, 172 axial slices, 256 × 256 in-plane, 1.0 mm isotropic). The T1-weighted images were processed using the Analysis of Functional NeuroImages (AFNI) software program to align each participant's brain with the MNI152_T1_1mm template. In AFNI, a mark was inserted in right intraparietal sulcus (coordinate: −22 70 58), which was used as the target for spTMS (see below).

spTMS Targeting and Delivery

spTMS targeting employed a navigated brain stimulation system that uses infrared-based frameless stereotaxy to coregister the location and position of the participant's head and that of the TMS coil according to the individual's high-resolution MRI (NexStim eXimia). spTMS was delivered with an eXimia TMS Focal BiPulse transcranial

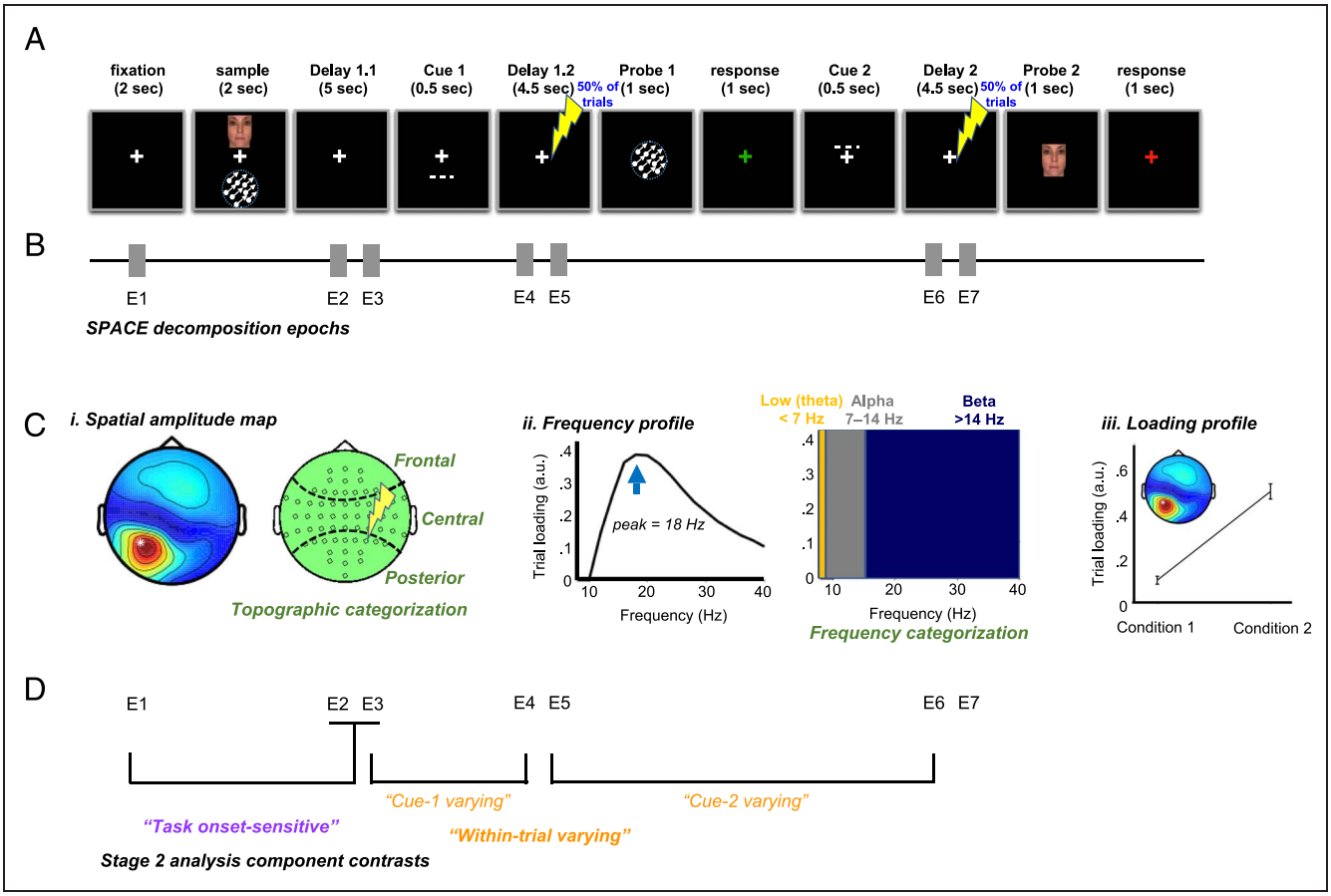

Figure 1. Methodological details. (A) Schematic of the DSR task. Memory sets were composed of two stimuli, one from each of three possible categories (faces, dot motion, and words). Schematic shows a trial in which a face is presented in the "up" location and a dot-motion patch in the "down" location. Participants were tested twice on each trial: On 50% of trials, they were tested on both items (as shown); on the other 50% of trials, they were tested on only one of the items (i.e., same location was cued twice, not shown). spTMS was delivered on 50% of trials during the delay periods preceding the probes. Participants made "match"/"nonmatch" responses to the probes and were provided feedback via the color of the fixation cross: green for correct responses (illustrated here following *Probe 1*) and red for incorrect responses (illustrated here following *Probe 2*). (B) Seven 1-sec epochs were extracted from each trial for spectral analysis and SPACE decomposition. (C) For each component, the procedure returned (i) a spatial amplitude map, (ii) a frequency profile, and (iii) a loading profile, which tracks variation in the component's prominence across time. Note that the lightning bolt icon specifies the electrode where spTMS was delivered, and the spatial amplitude map corresponds to a single component returned by the decomposition. (D) After categorization by topography and frequency, components were classified functionally. "Task onset-sensitive" components were those whose loading differed statistically between pretrial fixation (E1) and the average of the two *Delay 1.1* epochs (E2 and E3). "Within-trial varying" components were whose loadings differed statistically between late *Delay 1.1* and early *Delay 1.2* (E3 and E4; "*cue-1* varying") and/or between late *Delay 1.2* and early *Delay 2* (E5 and E6; "*cue-2* varying").

magnetic stimulator fit with a figure-of-eight stimulating coil. spTMS was delivered to the right intraparietal sulcus target in each participant to achieve an estimated intensity at the stimulation target of 90–110 V/m (60–75% of stimulator output, depending on the thickness of the participant's scalp, cortex, and depth of the target). The coil was oriented along the sagittal plane to induce an anterior–posterior direction of current, with individual adjustments to minimize EEG artifact. Stimulator intensity, coil position, and coil orientation were held constant for each participant for the duration of each session. spTMS was delivered 2–3 sec after cue offset (2.5–1.5 sec before probe presentation) in steps of 500 msec. To mask the sound of TMS coil discharge, participants were fitted with earbuds through which white noise was played during task blocks, with volume titrated such that the participants could not detect the click produced by coil discharge.

EEG Recording and Preprocessing

EEG was recorded with a 60-channel cap and TMS-compatible amplifier, equipped with a sample-and-hold circuit that held amplifier output constant from 100 μs before stimulation to 2 msec after stimulation (NexStim eXimia). Electrode impedance was kept below 5 kΩ. The reference electrode was placed superior to the supraorbital ridge. Eye movements were recorded with two additional electrodes, one placed near the outer canthus of the right eye, and one underneath the right eye. The EEG was recorded between 0.1 and 350 Hz at a sampling rate of 1450 Hz with 16-bit resolution.

Data were processed offline using EEGLAB (Delorme & Makeig, 2004) with the TMS-EEG signal analyzer open-source EEGLAB extension (Mutanen, Biabani, Sarvas, Ilmoniemi, & Rogasch, 2020; Rogasch et al., 2017) and Fieldtrip (Oostenveld, Fries, Maris, & Schoffelen, 2011) toolboxes in MATLAB. We followed the TMS-EEG analysis pipeline (https://nigelrogasch.github.io/TESA/). For delay periods for which no spTMS was delivered, a dummy spTMS event tag was added at a latency that matched the most recent spTMS-present trial delay period. Then, electrodes exhibiting excessive noise were removed and the data were epoched to −12 sec to 8 sec around the first spTMS event tag (*Delay 1.2*) and −4.5 sec to 4.5 sec around the second spTMS event tag (*Delay 2*). The data were down-sampled to 500 Hz. To minimize the TMS artifact in the EEG signal, the data were interpolated using a cubic function from −2 to 30 msec around the TMS pulse. This interpolation was also carried out on delay periods on which TMS was not delivered. Next, the data were band-pass filtered between 1 and 100 Hz with a notch filter centered at 60 Hz. Independent components analysis was used to identify and remove components reflecting residual muscle activity, eye movements, blink-related activity, residual electrode artifacts, and residual TMS-related artifacts. Electrodes with excessive noise were interpolated using the spherical spline method. Finally, the data were rereferenced to the average of all electrodes that were included in the independent components analysis.

The spTMS-related influence on the signal captured by the electrode directly below the TMS coil (P2) was assessed in three ways. First, spTMS-evoked potentials were extracted for the P2 channel using the TMS-EEG signal analyzer toolbox, for the data epoched to the first spTMS pulse and to the second spTMS pulse for each participant. These spTMS-evoked potentials were then averaged across participants, and a 95% confidence interval was computed for each time point. Two additional analyses were carried out on spectral transforms of the data—time–frequency representations (TFRs) and inter-trial phase coherence (ITC)—as described in the next two paragraphs.

Spectral transforms of the data were calculated for each participant with the FieldTrip toolbox, which resulted in TFRs epoched to the first spTMS pulse and to the second spTMS pulse, with spTMS-present and spTMS-absent trials transformed separately. (For spTMS-absent delay periods, analyses were time-locked to the same postcue timepoint at which spTMS had been delivered in the most recent trial during which spTMS had been delivered during that delay period.) A multi-taper-method convolution was performed on the epoched data. A fixed, three-cycle Hanning-tapered window of 50 msec was used for every other integer frequency from 8 to 40 Hz. Spectral estimates for each frequency were baseline corrected on a trial-by-trial basis by subtracting the mean spectral power from the 500-msec window preceding spTMS delivery. The resultant within-subject TFRs were then averaged across trials by condition (i.e., spTMS-present and spTMS-absent) and combined across participants. The two groups of TFRs were then submitted to a cluster-based permutation analysis to identify time–frequency clusters that differed significantly between the spTMS-present and spTMS-absent conditions. The analysis was carried out on the time window from 0 to 500 msec post-spTMS. Clusters were defined within the P2 electrode TFR in which the t statistic corresponding to the difference between spTMS-present and spTMS-absent trials between 0 and 500 msec post-TMS exceeded a threshold of $p < .025$ (for two-tailed t tests). Those exhibiting above-threshold differences were then used for the subsequent nonparametric cluster-based permutation analysis, which included 500 random sets of permutations. A significance value of 0.05 was used to threshold the cluster statistic.

ITC was calculated with the FieldTrip toolbox by applying wavelet decompositions epoched for each delay period around delivery of spTMS (or comparable time point for spTMS-absent delays, as with TFR analyses). A Morlet wavelet at every integer frequency from 4 to 40 Hz was used with a width of seven cycles. The Fourier spectra of the transform were returned. The ITC values were computed by dividing the Fourier spectra by the amplitude and then normalizing across trials. For any point in time, ITC values near 0 reflect high variability in phase angle across trials, whereas values near 1 reflect high consistency in the phase angle across trials.

Finally, the cleaned data were further divided into seven 1-sec epochs of interest per trial for the SPACE decomposition analyses (see below) and a multi-taper-method convolution was performed on the epoched data. A Hanning taper was applied to a four-cycle window at each integer frequency from 5 to 40 Hz, resulting in a frequency-dependent window length. This window was slid in 50-msec steps through each 1000-msec epoch. This transform resulted in spectral power values at each of 36 frequencies and 60 channels, sampled every 50 msec sec, for each 1-sec epoch. These data were used for the subsequent SPACE decomposition.

SPACE Decomposition

We employed SPACE, a model-based method that entails a signal decomposition application of parallel factor analysis to identify neurobiologically plausible rhythms and characterize "rhythmic components" by patterns of between-sensors phase coupling. Here, we describe the key aspects of the analysis pipeline. For a full description of the method, see van Der Meij and colleagues (2016) and van der Meij, Jacobs, and Maris (2015).

The SPACE decomposition was carried out for each participant ($n = 12$) and session ($n = 3$), resulting in 36 separate session-level decompositions. We focused the analysis on the seven 1-sec epochs of each trial within each session (Figure 1B): (i) fixation (baseline; E1; (ii–iii) mid- and late-*Delay 1.1* (before *Cue 1*; E2 and E3); (iv–v)

early- and late-*Delay 1.2* (following *Cue 1* and flanking the TMS pulse; E4–E5); and (vi–vii) early- and late-*Delay 2* (following *Cue 1* and flanking the TMS pulse; E6–E7). The Fourier coefficients for each epoch returned from the spectral analysis were used to compute frequency- and trial-specific cross-spectral density matrices (CSDs) that reflected both power at different electrodes and between-phases consistency.

To run the SPACE decomposition, we used the open-source MATLAB toolbox "NWAYDECOMP" (https://github.com/roemervandermeij/nwaydecomp). The frequency- and trial-specific CSDs were concatenated into a four-way array—*Channel* × *Channel* × *Frequency* × *Trial*—and then submitted to the decomposition procedure, which extracts the components using the iterative alternating least squares algorithm, "SPACE-FSP" (the frequency-specific phase model variant of the decomposition). Complete modeling details can be found in van der Meij and colleagues (2015). In brief, per alternating least squares iteration, four parameters sets (frequency profile, spatial amplitude map, spatial phase map, and trial profile; see below) are sequentially updated using ordinary least squares (with the exception of the spatial phase map, which requires a different optimization approach [van der Meij et al., 2016]), whereas the other three are held constant. The model is as follows:

$$X_{kl} \cdot X_{kl}^{*} = AL_k \cdot diagB_k \cdot diagC_l \cdot D_k \cdot diagC_l \cdot diagB_k \cdot AL_k^{*} + E_{kl}$$

The CSDs ($X_{kl} \cdot X_{kl}^{*}$) are modeled as a product of four matrices, of which three appear twice (AL_k, diag B_k, and diag C_l) and one appears only once (D_k). The difference between the model and the observed CSD is the error term E_{kl}. AL_k corresponds to the sensor-by-components matrix (with dimensions $J \times F$; where F is the number of components), which is complex-valued, and is formed by the spatial amplitude map (specifying the amplitudes of the complex numbers for each sensor j) and the frequency-specific spatial phase map (specifying the phases of the complex numbers) of each component. Diag B_k (with dimensions $F \times F$) is diagonal and real-valued, and contains a weighting ("loading") of components at frequency k. When concatenated over frequencies, the diagonals form the frequency-by-components matrix of frequency profiles B. Diag C_l (with dimensions $F \times F$) is diagonal and real-valued and contains the weighting (loading) of components in a trial l. When concatenated over trials, the diagonals form the trial-by-components matrix of trial profiles C. D_k (with dimensions $F \times F$) is denoted as a between-components coherency matrix that describes relations between components, is complex-valued and conjugates symmetric, and describes the phase coupling between components at frequency k.

The solution is not analytically defined, so the iterative approach is designed to extract statistically reliable components. An iteration is complete when all four parameter sets have been updated, upon which the increase in the quality of the fit is determined. Once subsequent iterations no longer increase the fit beyond a predetermined relative criterion, the algorithm is said to have converged and is stopped. On the basis of several test-runs of the procedure, we initialized the procedure to extract a starting number of components from the full data set (i.e., all epochs from the session-level data set being analyzed) to $n_1 = 18$ components. When the component extraction from the full data set had been completed, the data set was then split into two halves (odd and even trials) and components were extracted from each. If the split-half extractions were sufficiently correlated (based on a similarity coefficient criterion set to .7), then the procedure continued (iterated) by increasing the set number of components to be extracted in steps of two (i.e., $n_i = n_{i-1} + 2$), until the split-half extractions no longer met the established criterion. When the iteration failed, a final iteration occurred, extracting $n_{i-1} - 1$ components, which comprised the final set returned for the session-level data set.

Because of the computationally demanding nature of these analyses, we took advantage of the ability to compute the decompositions of all data sets in parallel, each employing MATLAB's pools of 12 "workers" using the HTCondor system deployed at the University of Wisconsin–Madison (Center for High Throughput Computing, 2006; https://doi.org/10.21231/gnt1-hw21).

As described above, the procedure fits four parameter sets. Upon completion, for each component extracted, SPACE generates four metrics according to the final optimized fit (Figure 1C): (i) a spatial amplitude map, indicating the loading on each channel for the component; (ii) a frequency profile, which describes the degree to which each frequency (in our analyses: 5–40 Hz) is involved in the phase coupling that characterizes the component; (iii) a loading profile, which describes the loading of that component (in arbitrary units, normalized to a scale of 1) at each epoch at the level of the individual trials; (iv) a spatial phase map that describes, per frequency, the between-sensors phase relations induced by the component source. Information from spatial phase maps was not used in this study.

Component Preselection

Topographic and Frequency Classification

We a priori planned to select beta components from two scalp locations (posterior and central) and alpha components from posterior locations, for subsequent analyses (Figure 1C and Table 1). For this initial stage of component preselection, a component's frequency category was based on the peak frequency in its frequency profile, with peak frequencies < 7 Hz being characterized as theta-band components, those with peak frequencies of 7–14 Hz as alpha-band components, and those > 14 Hz as beta-band components. Topography was characterized

Table 1. Topographical and Spectral Distribution of Components Extracted Using SPACE Decomposition of EEG Data

	Topography		
Frequency Range	*Posterior*	*Central*	*Frontal*
Low (theta) 5–7 Hz	107	32	25
Alpha 7–14 Hz	368	106	36
Beta > 14 Hz	115	52	21

based on the spatial amplitude map returned by the SPACE procedure. For each component, we found the peak channel in this map and categorized it as "posterior," "central," or "frontal" based on its location on the scalp (Figure 1C). (Note that the TMS coil was positioned over one of posterior channels [P2].) Once these classifications were complete, we visually inspected the spatial amplitude map and frequency profile of each posterior beta, central beta, and posterior alpha component, and manually rejected from subsequent analyses any that appeared to be artifactual, that is, exhibiting spatial patterns consistent with muscle or eye movement artifacts, and/or the frequency spectrum contained sharp discontinuities or multiple peaks.

Functional Classification

The second stage of our component preselection procedure involved a functional categorization that was based on sensitivity to different elements of the DSR task. We defined as "task onset-sensitive" those components with statistically significant differences in component loading between fixation (E1) and the average of mid- and late-*Delay 1.1* (E2 and E3; Figure 1D). This procedure was agnostic as to whether these modulations were increases or decreases from baseline. We defined as "within-trial varying" components with statistically significant differences in trial loading between late *Delay 1.1* and early *Delay 1.2* (E4 and E5; *"cue-1 varying"*), and/or between the late *Delay 1.2* and early *Delay 2* (E6 and E7; *"cue-2 varying"*; Figure 1D). Because a component could be both task onset-sensitive and within-trial varying, in initial analyses, those that had both properties were classified as task-onset sensitive.

Hypothesis-testing Analyses

We carried out three sets of statistical analyses to test hypotheses about posterior beta components: one about their sensitivity to spTMS and two about their contribution to WM. Note that because the contrasts used here did not overlap with the functional classification, we avoided the problem of "double-dipping." Our original plan was to carry out each set of hypothesis-testing analyses twice, once for task onset-sensitive components and once for within-trial varying components. However, results for the two types of component were similar for all analyses except one, and so in the Results section, unless otherwise noted, we report the results from the analyses on the combined pool of both types of "task-sensitive" components.

The spTMS-related Spectral Perturbation

The first set of analyses investigated the physiological effects of spTMS. In particular, we asked whether the spTMS-related spectral perturbation is best understood as resulting from the triggering of activity in previously "silent" circuits (i.e., an "activation" account), the modulation of patterns of activity in circuits that were active before the delivery of spTMS (i.e., a "modulation" account), or some combination of the two. We reasoned that a "spTMS-activated" oscillator would manifest as a component whose loadings met two constraints: (i) having a value close to 0 (operationalized as < 0.001) during the epoch(s) that immediately preceded spTMS (i.e., E4 and/or E6), and (ii) having a nonzero value (operationalized as > 0.001) during the epoch(s) immediately following spTMS (i.e., during E5 and/or E7, respectively). As a control, to determine how often a SPACE component might exhibit this pattern by chance, we performed the same analysis for spTMS-absent trials and compared the two.

The Dynamics of Low-frequency Components across the DSR Task, and Their Sensitivity to spTMS

The second set of analyses investigated the task-related and spTMS-related dynamics of posterior beta components. To quantify task-related variability, we fit a linear mixed-effects model to the posterior beta component loadings of early and late *Delay 1.2* (i.e., E4 and E5) and *Delay 2* (i.e., E6 and E7). Main effects of (i) epoch (two levels: early; late) and (ii) delay period (two levels: *Delay 1.2* and *Delay 2*) were included in the analysis as fixed effects. Both variables were coded as categorical variables. As random effects, the model included intercepts for individual components. (Note that for the purpose of this set of analyses, the full set of components was pooled across participants, thereby ignoring the factor of participant.) To quantify the spTMS-related dynamics of posterior beta, we

fit a linear mixed-effects model to the posterior beta component loadings of the late-delay epochs: E5 and E7. Main effects of (i) spTMS delivery (two levels: present; absent) and (ii) delay period (two levels: *Delay 1.2* and *Delay 2*) were included in the analysis as fixed effects. Both variables were coded as categorical variables. As random effects, the model included intercepts for individual components. Visual inspection of residual plots did not reveal any obvious deviations from homoscedasticity or normality for either model. Both models were fit both with and without the interaction terms (i.e., between delay period and epoch for the first model and between spTMS delivery and delay period for the second model). The interaction was not significant, and the overall fit of the model was worse when the interaction was included in both cases, so we report the results from the non-interaction models. p Values were obtained from F tests for each term in the linear mixed-effects models. Post hoc comparisons testing for statistically significant differences between pairs of epochs (E4 vs. E5 and E6 vs. E7), and testing for effect of spTMS in specific delay periods were carried out using paired-samples t tests. Finally, the model fitting was repeated for the posterior alpha and central beta components.

Relating the Effects of spTMS on Posterior Beta Components to Behavior

For this third set of analyses, we first calculated the percentage change in posterior beta trial loadings between early and late epochs of the delay periods (i.e., from E4 to E5 and E6 to E7, computed as ((early-late)/early) $\times 100$), then we fit linear mixed-effects models to accuracy (% correct) across trials. Main effects of (i) percentage change in trial loading across the delay period (continuous variable), (ii) spTMS delivery (two levels: present, absent; categorical variable), and (iii) delay period (two levels: *Delay 1.2* and *Delay 2*; categorical variable) were included in the analysis as fixed effects. Because each participant had a single accuracy measurement for each combination of spTMS delivery and delay period (e.g., % correct for *Probe 1* responses when spTMS was delivered during *Delay 1.2*), we computed the median% change in trial loadings across all components extracted for a given participant for each spTMS delivery + delay period combination, and paired with the corresponding accuracy for analysis. Interaction terms were not included in the models, and p values were obtained from F tests for each term in the linear mixed-effects model. We repeated the same analysis for posterior alpha and central beta components.

Finally, we focused on the 10% of delay–probe pairs for which the UMI served as the probe (i.e., as a lure). These have distinct theoretical importance, because worse performance on these probes following spTMS (Fulvio & Postle, 2020; Rose et al., 2016) provides evidence for a functional consequence of the spTMS reactivation effect. Specifically, results from *Delay 1.2 and Probe 1* pairs demonstrate that not only does spTMS rescue decodability of the UMI in the EEG, it also increases the UMI's influence on behavior, suggesting that spTMS effects a true change of its priority status of the UMI within WM. For this analysis, we fit a linear mixed-effects model to accuracy from *delay–probe* pairs that presented the UMI as the probe. As with the previous analyses, percentage change in component loading was used as a fixed effect term. In addition, we included an interaction term between TMS delivery and delay period, because previous analysis of this data set found that the false-alarm rate to lures was elevated when spTMS was delivered during *Delay 1.2*, but not during *Delay 2*, nor during *Delay 1.2* on a single-retrocue control task for which, unlike the DSR, the uncued item could be dropped from WM (rather than held as a UMI) during *Delay 1.2* (Fulvio & Postle, 2020). (Note that this analysis would necessarily feature many fewer trials than the analysis including all trials, and so would be less sensitive.) We repeated this analysis for posterior alpha and central beta components.

RESULTS

We begin with a descriptive summary of low-frequency components identified via the SPACE decomposition, followed by the three sets of hypothesis-testing analyses.

Categorization of Extracted Components

Topographic Categorization

Eight hundred twenty-one components with peak frequencies in the 5–7 Hz (theta); 7–14 Hz (alpha) and 14–40 Hz (beta) bands were extracted from the 36 EEG data sets (12 participants $\times$ 3 sessions). For each frequency category, the majority of the components were localized to posterior areas of the scalp (Table 1). For the remainder of this report, our emphasis is on posterior components in the beta band; see Appendix for details of the categorization of central beta-band components and posterior alpha-band components.

Functional Categorization

After manual artifact rejection, 103 posterior beta components remained, 50 of which were identified as task onset-sensitive (44 were up-modulated), and 28 were within-trial varying (but not task onset-sensitive) components (Figure 2). Finally, 25 components showed neither task onset sensitivity nor within-trial variability, and were excluded from further analysis. For the final set of 78 posterior beta components included in our analysis, each participant contributed from 2 to 15 components (mode = 9; see Table 2 for functional categorization breakdown). We carried out the same component preselection procedures for the posterior alpha and central beta components (see Appendix).

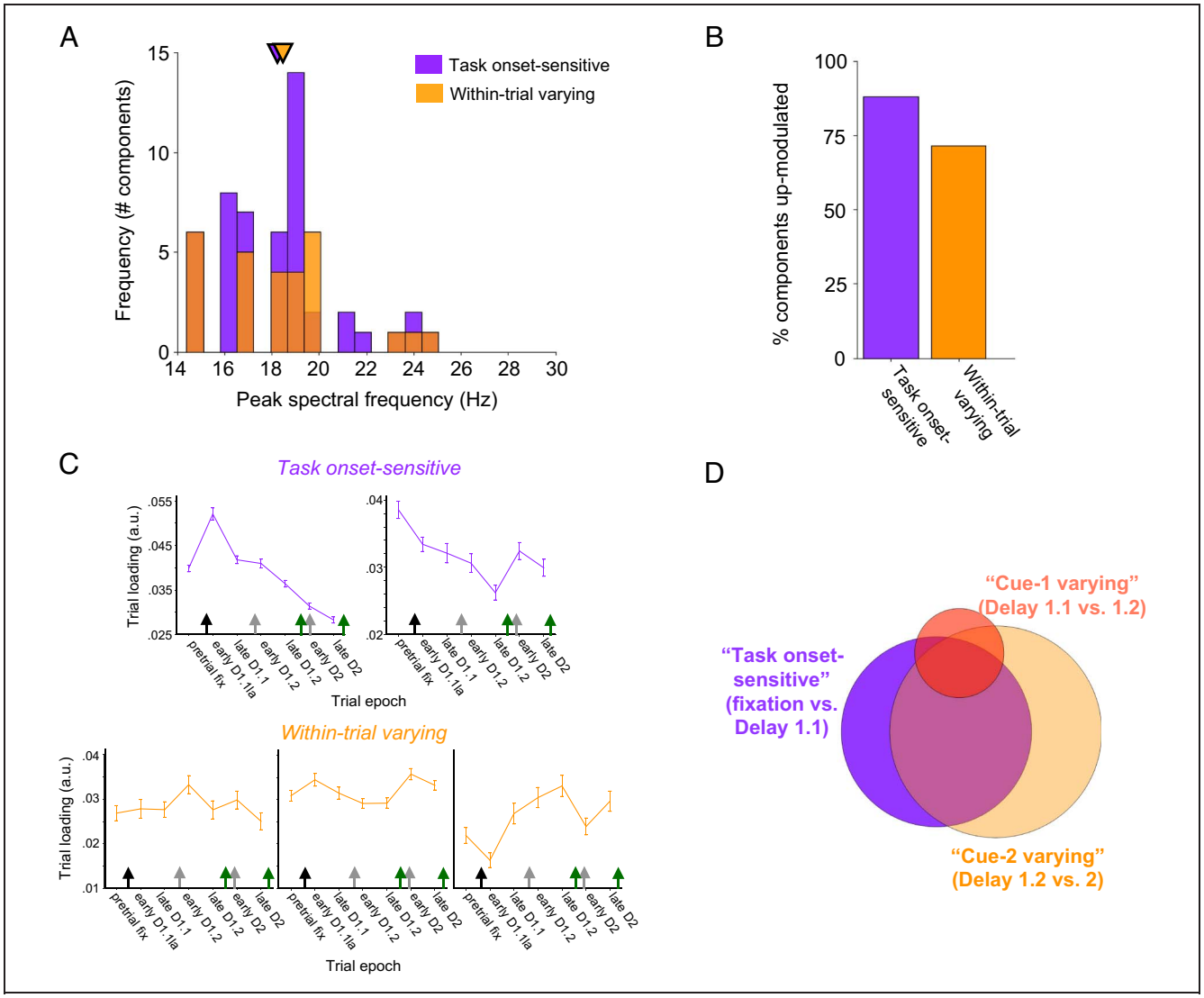

Figure 2. Characteristics of selected posterior beta components. (A) Peak spectral frequency (Hz) distribution for the 50 task onset-sensitive components (purple) and the 28 components with exclusively within trial-varying properties (orange). The triangles denote the mean peak frequency for the two groups (18.22 Hz and 18.39 Hz, respectively). (B) The bar graph depicts the percentage of components up-modulated for the two categories, with up-modulation corresponding to greater loading for *Delay 1.1* than fixation for task onset-sensitive components, and greater loading for early *Delay 1.2* than late *Delay 1.1* and for early *Delay 2* than *late Delay 1.2* for within trial-varying components. (C) Trial loading time courses for individual components that illustrate each of five characteristic patterns: task onset-sensitive, up-modulated (top row, left); task onset-sensitive, down-modulated (top row, right); within trial-varying *Cue 1* up-modulated (bottom row, left); within trial-varying Cue 2 up-modulated (bottom row, middle); within trial-varying *Cue 2* down-modulated (bottom row, right). Black arrows indicate sample presentation; gray arrows indicate cue presentation; green arrows indicate probe presentation. (D) Distribution of overlap among the three component types. Note that 25 components did not survive any of the thresholding procedures.

Table 2. Breakdown of Posterior Beta Components

	Posterior Beta Component Classification				
	Task Onset-sensitive	*Within-trial Varying*	*Cue-1 Varying*	*Cue-2 Varying*	*Residual*
Total classified	50	65 (w/ overlap); 28 (w/o overlap)	11; 1	62; 27	25
Participant contributions	0–8 $M = 4.2$	0–6 $M = 2.3$ (w/o overlap)	0–1 $M = .1$ (w/o overlap)	0–6 $M = 2.3$ (w/o overlap)	0–5 $M = 2.1$

The extracranial EEG arises from the blending of multiple underlying sources (Nunez & Srinivasan, 2006). SPACE decomposition quantifies these as a spatially and spectrally diverse set of components exhibiting varying levels of sensitivity to task demands. Notably, only a subset of these sources display task sensitivity. For the hypothesis-testing analyses that follow, we focus only on task-sensitive components. Furthermore, we present the results of the statistical analyses carried out with task onset-sensitive and within-trial varying component types combined as a group, because the results were not appreciably different when the analyses were performed on the groups separately, except where noted.

Physiology of the spTMS-related Spectral Perturbation

This set of hypothesis-testing analyses addressed the question of whether the spTMS-related spectral perturbation of the EEG is better understood as resulting from an "activation" or a "modulation" mechanism. They were based on the reasoning that an "activation" mechanism would manifest as a SPACE component with negligible component loading during the epoch immediately before delivery of spTMS, but a robust component loading during the epoch immediately after the delivery of spTMS. Alternatively, a "modulation" mechanism would manifest as a change in component loadings that were already elevated before spTMS delivery.

We carried out our investigation of the spTMS-related spectral perturbation on the signal captured by the electrode directly below the TMS coil. As illustrated in Figure 3, spTMS produced an average evoked response spanning from ~−2 μV to ~2 μV and largely resolving within 250 msec. The TFR of this response contained an early, short-duration broadband response (a "spike" that is likely a byproduct of the fast Fourier transform of the initial voltage transient) and a burst of elevated power spanning roughly 7–20 Hz for roughly the first 150 msec and narrowing to the theta band for an additional roughly 200 msec. ITC showed a similar profile: a broadband spike followed by elevated values spanning from roughly 5–20 Hz, with peak values in the theta band.

Turning to SPACE components, we first inspected posterior beta component loadings on a trial-by-trial basis during spTMS-present delay periods. Negligible pre-spTMS component loadings (i.e., loadings < .001) were identified for 4.57% of *Delay 1.2* epochs (M = .00002, SD = .0001) and for 6.96% of *Delay 2* epochs (M = .0001, SD = .0002). For these trials, the average post-spTMS component loadings were .0222 (SD = .0198) for *Delay 1.2* and .0129 (SD = 0.0161) for *Delay 2*. If considered alone (i.e., at face value, without comparison to the control condition), these results might imply that only a small proportion of trials (less than 7%) show evidence that could be consistent with an activation account of the spTMS-evoked response. Importantly, however, repeating this procedure with the same set of components but during spTMS-absent delay periods revealed that this pattern was also present on roughly the same proportion of delay periods: *Delay 1.2*: 4.5% of trials; *Delay 2*: 6.64% of trials. We repeated the same procedure for posterior alpha and posterior theta component loadings. We found that a markedly higher percentage of these had negligible pre-spTMS component loadings (alpha: 40.12% of *Delay 1.2* epochs and 43.32% of *Delay 2* epochs; theta: 46.33% of *Delay 1.2* epochs and 51.77% of *Delay 2* epochs). However, as observed for posterior beta components, similar proportions were observed during spTMS-absent delay periods (alpha: 40.45% of *Delay 1.2* epochs and 43.74% of *Delay 2* epochs; theta: 45.5% of *Delay 1.2* epochs and 53.97% of *Delay 2* epochs).

These results represent a failure to find evidence for an "activation" account of the spTMS-related spectral perturbation. By implication, we conclude that the spTMS-related spectral perturbation may be best understood as arising from the modulation of activity in ongoing sources of oscillatory activity. The precise nature of this modulation is the focus of the next section of the Results.

Dynamics of Low-frequency Component Loadings across Delay Periods, and Their Sensitivity to spTMS

We now turn to a detailed assessment of how spTMS modulates delay-period activity during the DSR WM task, with the results summarized in Figure 4. Beginning with posterior beta components, a linear mixed-effects model revealed a significant main effect of delay-period epoch, that is, early versus late; $F(1, 309) = 27.206, p < .001$, with loadings decreasing across both *Delay 1.2* and *Delay 2* ($p < .001$ for both). A second linear mixed-effects model revealed a significant main effect of spTMS, $F(1, 309) = 7.9977, p = .004$, on late-delay period loadings, with late-delay loadings lower for spTMS-present than spTMS-absent delay periods ($p < .001$ for both delays; Figure 4A). In addition, the linear mixed-effects model revealed a significant main effect of delay period, $F(1, 309) = 15.451, p < .001$, reflecting the fact that late-delay period loadings were higher during *Delay 1.2* than during *Delay 2*. A similar pattern of results was observed when posterior beta components were split according to whether they were up-modulated or down-modulated within the contrast used to categorize them (see Appendix). Therefore, for posterior beta component loadings, for both delays, the trend was that they declined across the delay period and that spTMS had the effect of enhancing this reduction.

Turning to posterior alpha components, although they showed a qualitatively similar pattern of component loadings within and across delay periods, they did not show sensitivity to spTMS. Specifically, although a linear mixed-effects model revealed a significant main effect of delay period epoch, that is, early versus late; $F(1, 989) =$

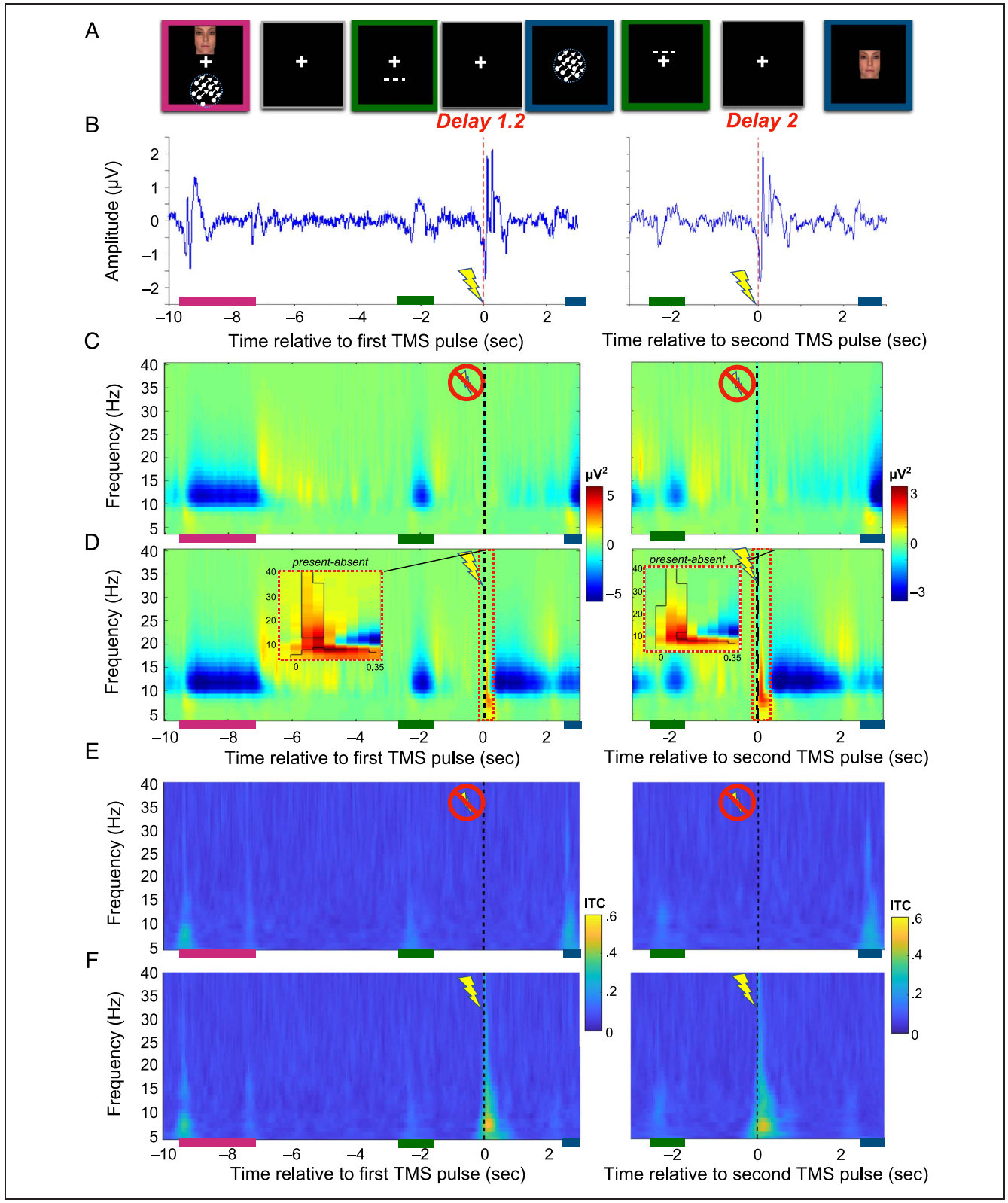

Figure 3. spTMS-related perturbations of the signal measured from the electrode under the coil. (A) Color-coded task schematic for reference in B–F. (B) spTMS evoked potentials. (C) Time–frequency spectral characteristics time-locked to the first TMS pulse (left column) and to the second TMS pulse (right column) for trials in which spTMS was not delivered. (D) Same as B but for trials in which spTMS was delivered. The insets illustrate the difference between the two conditions (spTMS-present – spTMS-absent) from 50 msec before spTMS to 350 msec post-spTMS. Statistical contrasts of the differences in these time windows reveal positive clusters spanning the theta to beta frequency ranges. (E) ITC for trials in which spTMS was not delivered (top) time-locked to the first TMS pulse (left column) and to the second TMS pulse (right column). (F) Same as E but for trials in which spTMS was delivered. Note that because of jitter in spTMS delivery (within 1 sec across trials), there is small temporal variation in other task components relative to the pulse.

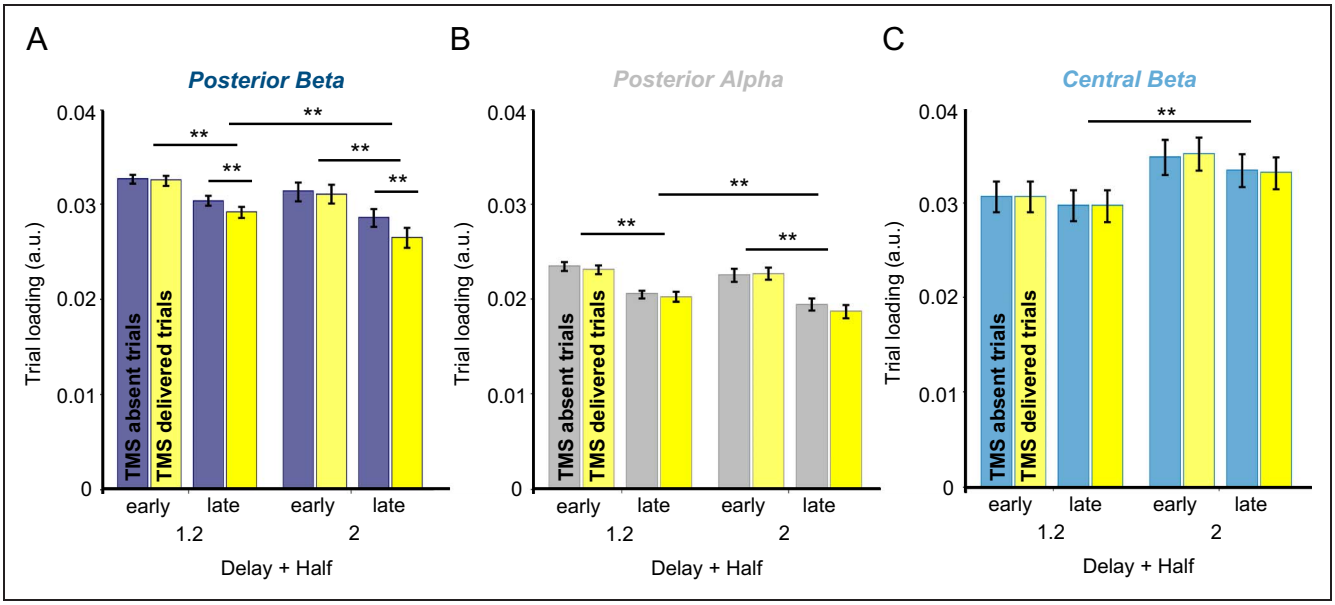

Figure 4. Component loadings as a function of trial epoch and spTMS delivery. (A) For posterior beta components, loadings declined from *Delay 1.2* to *Delay 2* and from early-to-late across both delay periods when spTMS was absent, and this effect that was exaggerated when spTMS was delivered. (B) Posterior alpha components exhibited task-related decrease of component loadings from *Delay 1.2* to *Delay 2*, and from early-to-late within both delay periods. They did not, however, show sensitivity to spTMS. (C) Central beta component loadings increased from *Delay 1.2* to *Delay 2*, but exhibited no other variation related to task or to spTMS. Error bars correspond to ± 1 *SEM* across the number of components; $^{**}p < .01$. Blue (A and C) and gray bars (B) correspond to trials in which TMS was not delivered; yellow bars correspond to trials in which TMS was delivered (all columns).

44.21, $p < .001$, because of loadings declining from the early- to late-delay period epochs ($p < .001$ for both delays), a second linear mixed-effects model revealed no effect of spTMS on late-delay period epoch loadings, $F(1, 989) = 0.988$, $p = .321$ (Figure 4B). Finally, as was the case for posterior beta, a linear mixed-effects model revealed a significant main effect of delay period, $F(1, 989) = 7.172$, $p = .008$, such that late-delay period loadings were higher during *Delay 1.2* than during *Delay 2*.

The dynamics of central beta components were markedly different from those of the posterior components. First, a linear mixed-effects model revealed no effect across delay periods, that is, early versus late; $F(1, 117) = 0.629$, $p = .429$. Second, a separate linear mixed-effects model revealed no effect of spTMS on the late-delay period loadings for these components, $F(1, 117) = 0.015$, $p = .902$ (Figure 4C) but did reveal a significant main effect of delay period, whereby late-delay period loadings were higher during *Delay 2* than during *Delay 1.2*, $F(1, 117) = 4.778$, $p = .031$.

To summarize, posterior components in the beta and alpha bands followed a general profile of declining from *Delay 1.2* to *Delay 2*, and from early to late across both delay periods. These results, suggesting involvement in the WM task, are broadly consistent with the previous report that the content of to-be remembered information can be decoded from EEG data bandpass filtered for these frequency bands (Rose et al., 2016). These two sets of components differed, however, in that only posterior beta components were sensitive to spTMS, with spTMS having the effect of exaggerating the across-delay decline in component loadings. One possible implication of this latter result is that it may correspond to the pattern of modulation that underlies the spTMS-triggered recovery of the decodability of the UMI. This speculation would receive further support if, in the final set of analyses (below), this effect of spTMS is shown to relate to behavior on the DSR WM task. (The dynamics of central beta components showed sensitivity to neither time within the delay period nor to spTMS.)

Relating spTMS Modulation of Low-frequency Components to Task Performance

The first two sets of hypothesis-testing analyses established that the spectral perturbation produced by spTMS is likely because of modulation of ongoing oscillatory activity and that during the delay periods of the DSR task only posterior beta components are sensitive to spTMS. In this final set of hypothesis-testing analyses, we assessed evidence for links between changes in component loadings and variation in performance on this task, and whether these interact with spTMS. The first step was important to do because it would further validate the assumption that the SPACE decomposition method yields components that can be analyzed to assess questions about brain–behavior correlation. The second was important because it could provide a stronger support for the plausibility of the idea that a "modulation" mechanism might underlie the spTMS-triggered involuntary retrieval effect.

Because the dominant pattern in the data was for component loadings to decrease across each delay period (Figure 4), we entered loading dynamics into the model as (early – late), such that a larger positive number would correspond to a larger drop in loading across the delay period. For posterior beta components, the linear mixed-effects model identified a significant negative relationship between the early-to-late decrease in component loading and behavioral accuracy, that is, the bigger the early-to-late decrease in component loading, the bigger the decline in performance; $F(1, 118) = 4.6331$, $p = .033$. When delay periods were broken out by spTMS condition, however, this relationship was seen to hold only when spTMS was delivered, spTMS-present: $F(1, 57) = 7.453$, $p = .008$; spTMS absent: $F(1, 59) = .267$, $p = .607$ (Figure 5A).

For posterior alpha components, we found no evidence for a relationship between the decrease in component loading and behavioral accuracy, whether assessed across all delay periods, $F(1, 139) = 1.6418$, $p = .202$, or separately for spTMS-present, $F(1, 68) = 3.0064$, $p = .087$, and spTMS-absent delay periods, $F(1, 68) = 0.04372$, $p = .835$ (Figure 5B). For central beta components, we found a relationship between the decrease in component

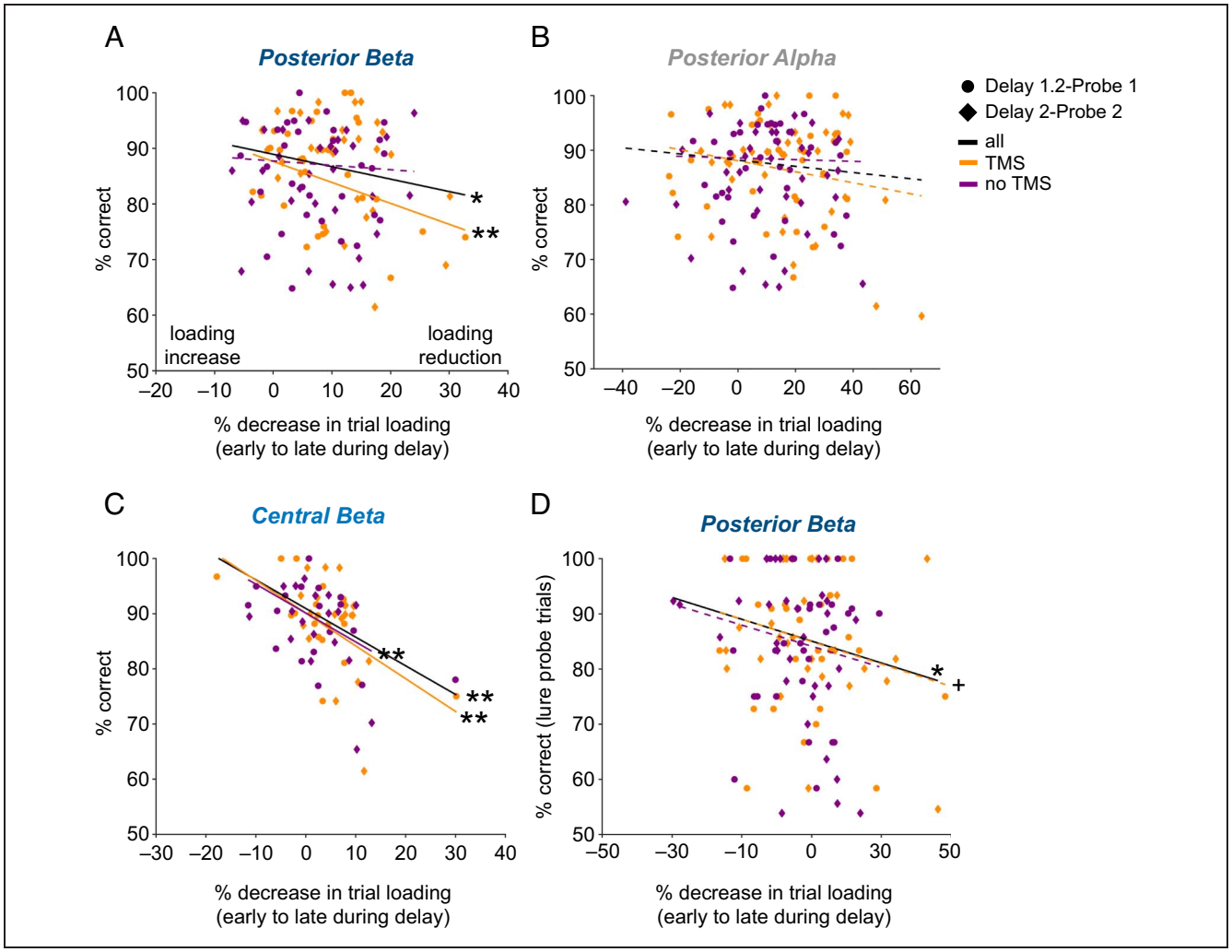

Figure 5. Relationship between delay-period component modulation and response accuracy for the subsequent probe, collapsed across component types. (A) Posterior beta components: Recognition accuracy declined with greater decrease in component loading from early-to-late portions of the delay period; solid black line shows significant fit for all delay–probe pairings, solid orange line shows significant fit for only spTMS-present, delay–probe pairings, dashed purple line shows nonsignificant fit for spTMS-absent, delay–probe pairings. (B) Posterior alpha components: no relation between accuracy and component dynamics. (C) Central beta components: Recognition accuracy declines with greater decrease in component loading from early-to-late epochs of the delay period, with fits significant and comparable whether calculated across all delay–probe pairings, only spTMS-present pairings, or only spTMS-absent pairings. (D) Posterior beta component modulations preceding lure probes: Recognition accuracy declined with greater decrease in component loading from early-to-late portions of the delay period when assessed across all trials, and approached significance for spTMS-present trials, but not for spTMS-absent trials. Each data point corresponds to a single participant + session combination. Circular symbols correspond to data points from *Delay 1.2 to Probe 1* pairings; diamond symbols correspond to data points form *Delay 2 to Probe 2* pairings. Orange symbols correspond to data points from spTMS-present delays; purple symbols correspond to spTMS-absent delays. Solid lines correspond to significant model fits; dashed lines correspond to nonsignificant model fits. Black lines correspond to model fits when trials are pooled across spTMS condition. $^{**}p < .01$, $^{*}p < .05$, $^{+}p < .10$.

loading and behavioral accuracy in the same direction as for posterior beta components, $F(1, 69) = 23.592$, $p < .001$ (Figure 5C). At variance with posterior beta components, however, this effect was present both for spTMS-present, $F(1, 34) = 13.359$, $p < .001$, and spTMS-absent, $F(1, 32) = 8.3655$, $p = .007$, delay periods. These results provide important validation of the assumption that, for a WM task, the SPACE decomposition procedure identifies components that reflect brain processes that can influence behavior. Furthermore, they lend further support to the idea that oscillatory dynamics in the beta band might be of particular importance for the encoding of priority in WM.

Finally, we focused on the subset of trials with lure probes because these are how we operationalize the behavioral phenomenon of spTMS-triggered involuntary retrieval. (Note that lure probes comprised 20% of trials, and so this set of analyses features decreased statistical power.) Beginning with posterior beta components, the linear mixed-effects model identified a significant negative relationship between the early-to-late decrease in component loading and behavioral accuracy on the lure-probe trials, $F(1, 118) = 4.5915$, $p = .034$, but no delay period by spTMS delivery interaction, $F(1, 118) = 0.0857$, $p = .77$. When broken out by spTMS condition, the relationship showed a trend for spTMS-present *Delay 1.2 and Probe 1 pairings,* $F(1, 59) = 3.1944$, $p = .079$, but not for spTMS-absent *Delay 1.2 and Probe 1 pairings,* $F(1, 58) = 1.5617$, $p = .22$ (Figure 5D).[4]

For posterior alpha components, we identified a significant negative relationship between the early-to-late decrease in component loading and behavioral accuracy, $F(1, 137) = 6.4934$, $p = .012$, and no delay period by spTMS delivery interaction, $F(1, 137) = 0.5043$, $p = .479$. When broken out by spTMS condition, the effects failed to achieve significance for delay–probe pairings when spTMS was delivered, $F(1, 68) = 2.8755$, $p = .095$, and when spTMS was not delivered, $F(1, 68) = 3.6707$, $p = .059$.

For central beta components, we found no main effect, $F(1, 69) = 0.1618$, $p = .689$, and no delay period by spTMS interaction, $F(1, 69) = 0.0898$, $p = .765$. When broken out by spTMS condition, no relationship was observed for spTMS-present, $F(1, 34) = 3.036$, $p = .09$, or spTMS-absent, $F(1, 34) = 1.8209$, $p = .186$, delay–probe pairings.

This final set of results provides further evidence consistent with the idea that the spTMS-triggered involuntary retrieval effect arises from beta-band dynamics, possibly as a consequence of the perturbation of a beta-band mechanism that holds the UMI in an unprioritized state. We elaborate on this idea in the Discussion section.

DISCUSSION

Previous results showing that a pulse of TMS can rescue the decodability of an UMI and that this effect can be isolated to the beta-band of the EEG, call for a better understanding of how spTMS influences brain activity in a manner that influences WM behavior. In the present study, we used a method that decomposes the EEG signal into a set of discrete coupled oscillators (SPACE), applying it to data from an spTMS-EEG study of the DSR WM task. Focusing on beta-band components localized to the posterior of the scalp, we found no evidence that spTMS activates previous "silent" sources. Rather, our results suggest that the spTMS-related spectral perturbation may be best understood as resulting from abrupt changes in the dynamics of activity that was already present in the signal before its delivery, a "modulation" account. Across the DSR task, the overall pattern was for the magnitude of posterior, low-frequency oscillators to decline across each delay period, with only beta-band oscillators additionally sensitive to spTMS, which had the effect of amplifying the decline. Furthermore, individual differences in the amplitude of the spTMS-related influence on posterior beta components predicted its effect on behavior. These results are consistent with the idea that prioritization in WM may be accomplished, in part, by a reconfiguration of beta-band dynamics and that spTMS can influence behavior by perturbing this reconfiguration in a manner that weakens the priority coding of stimulus information, thereby facilitating involuntary retrieval of the UMI.

In the skeletomotor system, the beta band is most often ascribed an inhibitory function. For example, the attenuation of oscillatory power in the beta-band (~14–30 Hz) recorded by EEG electrodes at central locations on the scalp, and contralateral to the response hand, is a well-established neural marker of manual action planning and execution (e.g., van Wijk, Daffertshofer, Roach, & Praamstra, 2009; Baker, 2007; Neuper, Wörtz, & Pfurtscheller, 2006; McFarland, Miner, Vaughan, & Wolpaw, 2000; Salmelin & Hari, 1994). Invasive recordings implicate primary motor cortex as an important source of these movement-related oscillatory dynamics (e.g., de Hemptinne et al., 2013; Kilavik, Confais, Ponce-Alvarez, Diesmann, & Riehle, 2010). Outside the skeletomotor system, beta-band oscillations have been associated with several aspects of perceptual and cognitive processing, and not all of them well characterized as "inhibitory." For example, beta-band activity has been linked to such functions as maintaining the existing cognitive set (Engel & Fries, 2010), selecting a rule (Buschman, Denovellis, Diogo, Bullock, & Miller, 2012), activating a stimulus representation (Spitzer & Haegens, 2017), (re-)activating relevant neural ensembles maintaining contextually defined categorical decisions (Rassi et al., 2023), inhibition of cognitive representations (Wessel & Anderson, 2024), and helping to stabilize working memory representations against disruption (Kornblith, Buschman, & Miller, 2016; Kundu, Chang, Postle, & Van Veen, 2015; Pereira & Wang, 2015). Models of predictive coding in perception identify the beta band as a critical frequency channel for the top–down propagation of prediction signals (Bastos et al., 2012, 2015). Our results add to this literature, suggesting a role in the encoding of priority status in WM.

Although it was previously hypothesized that the UMI may be held in an "activity-silent" state (e.g., Rose et al., 2016), more recent work has shown the UMI to be held in a state that, although active, is transformed relative to when it has prioritized status (Wan et al., 2020; Yu, Teng, & Postle, 2020). Furthermore, computational simulations suggest that this transformation can be implemented via the stratification of the stimulus-representing subspace into "activity-potent" versus "activity-null" representational substrata (Wan et al., 2024), the latter perhaps corresponding to a configuration that is not amenable to read out for the influence of behavior. One implication of these developments is that it is no longer necessary to hypothesize a mechanism for spTMS whereby it activates previously "activity-silent" stimulus representations (cf. Rose et al., 2016). This theoretical evolution receives further support from the present results, in part because they failed to find evidence for the "activation" mechanism of spTMS on which the "activity-silent" account depended.

If spTMS works by modulating ongoing oscillatory dynamics, as suggested by the results of this study, how can this be reconciled with its functional effect of triggering involuntary retrieval of the UMI? In the DSR task, *Cue 1* prompts a change in the functional status of both memory items: The cued item becomes prioritized (relevant for the impending memory probe), and the uncued item becomes unprioritized (not relevant for the impending memory probe, but possibly relevant for the subsequent one). On the basis of the current results, we speculate that this priority-based coding may be implemented and maintained, in part, by a reconfiguration of ensembles oscillating in the beta-band. Such a scheme could reflect, for example, a generalization of the model described by Miller and colleagues (e.g., Bastos, Loonis, Kornblith, Lundqvist, & Miller, 2018; Miller, Lundqvist, & Bastos, 2018; Lundqvist et al., 2016) whereby beta-band oscillations in deep layers of pFC act to "close the gate" and protect the current configuration of synaptic weights from being overwritten by incoming information carried in gamma-frequency bursts. From this perspective, the spTMS-related decreases in posterior beta component loadings described in the present report may reflect an alteration, perhaps a weakening, of the priority-based configuration that is critical for distinguishing prioritized memory item from UMI status. Involuntary retrieval of an already-potent lure would be a consequence of this blurring of the representation of which of the two memory items is the one that was most recently cued.

APPENDIX

SPACE Component Preselection—Posterior Alpha Component Characteristics

The manual inspection procedure resulted in the removal of 47 posterior alpha-classified components (11.1%), with 327 components remaining (see Figure A1 and Table A1). One hundred thirteen task onset-sensitive components were identified by contrasting trial loadings during pretrial fixation versus Delay 1.1, when two items were held in working memory, which had an average peak frequency of 11.21 Hz (*SD* = 1.69 Hz). Seventy-six task onset-sensitive posterior alpha components exhibited an increase in loading (65.5%), and nine exhibited a decrease in loading.

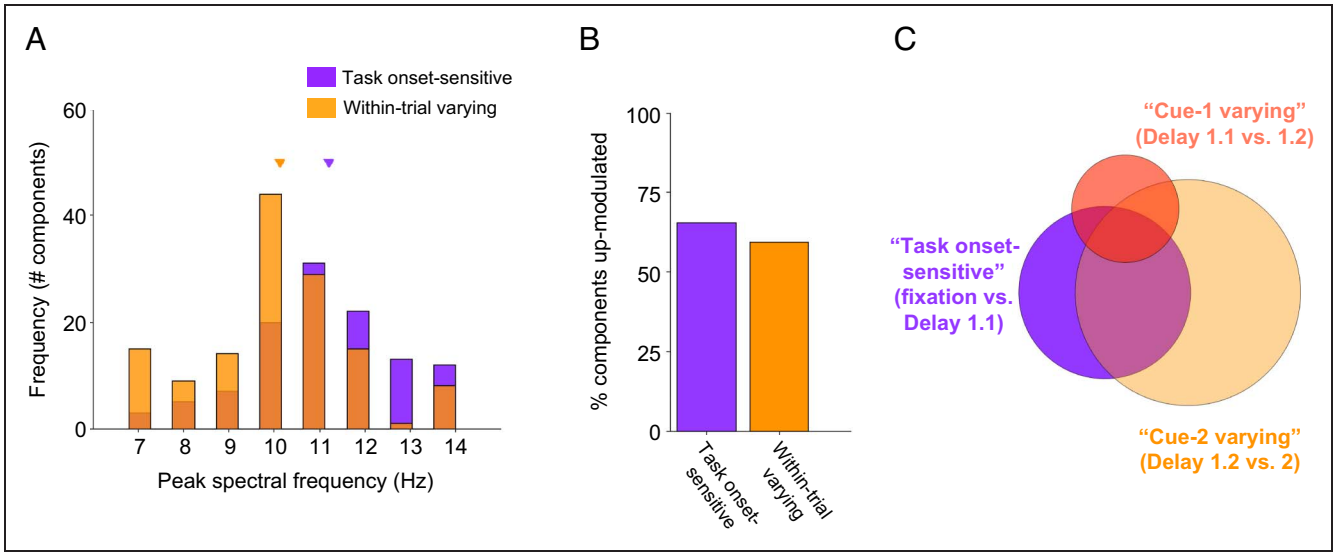

Figure A1. Characteristics of posterior alpha components selected for the primary analyses. (A) Peak spectral frequency (Hz) distribution for the set of 113 task onset-sensitive components (purple) and for the set of 135 non-overlapping within-trial varying components (orange). The triangles denote the mean peak frequency for the two groups = 11.21 Hz and 10.13 Hz, respectively. (B) Percentage of components up-modulated for the two sets of components, with increases reflecting greater loading during Delay 1.1 after the sample in comparison to fixation for task onset-sensitive components, and greater loading during early Delay 1.2 compared with late Delay 1.1 and early Delay 2 compared with late Delay 1.2 for within-trial varying components. (C) Distribution of overlap among the three component types. Note that 89 components did not survive any of the thresholding procedures.

Table A1. Breakdown of Posterior Alpha Components

	Posterior Alpha Component Classification				
	Task Onset-sensitive	*Within-trial Varying*	*Cue 1-Varying*	*Cue 2-Varying*	*Residual*
Total classified	113	214 (w/ overlap); 135 (w/o overlap)	44; 23	194; 112	89
Participant contributions	2–18 $M = 9.4$	4–19 $M = 11.3$ (w/o overlap)	0–7 $M = 3.75$ (w/o overlap)	9–29 $M = 16.2$ (w/o overlap)	2–15 $M = 7.4$

Forty-four within-trial varying components were identified by contrasting trial loadings between Delay 1.1 and Delay 1.2 ("Cue 1-varying"), and 194 within-trial varying components were identified by contrasting trial loadings between Delay 1.2 and Delay 2 ("Cue 2-varying"). Like the posterior beta components, the three sets of posterior alpha components overlapped considerably—the 135 components that were identified only in the within-trial contrasts related to the cues were included as the within-trial varying component set.

The average peak frequency of the within-trial varying components was 10.13 Hz ($SD = 1.75$ Hz), which was significantly slower in frequency relative to that of the task onset-sensitive posterior alpha components, $t(246) = 4.9158$, $p < .001$. Eighty within-trial varying components had an increase in loading (59.3%), and 55 had a decrease, a relative proportion that did not vary from the task onset-sensitive posterior alpha components, $\chi^2(1) = 0.7662$, $p = .381$.

Eighty-nine of the posterior alpha components were not identified by any of these contrasts and were excluded from further analysis. For the final set to be analyzed, each participant contributed 12–37 components with a mode contribution of 16. The resulting set of posterior alpha components were analyzed using the primary statistical analyses of interest to serve as a basis for comparison/control in interpretation of the results from the posterior beta components.

SPACE Component Preselection—Central Beta Component Characteristics

The manual inspection procedure resulted in the removal of 14 central beta-classified components (26.9%), with 38 components remaining (see Figure A2 and Table A2). Eleven task onset-sensitive components were identified by contrasting trial loadings during pretrial fixation versus Delay 1.1, when two items were held in working memory,

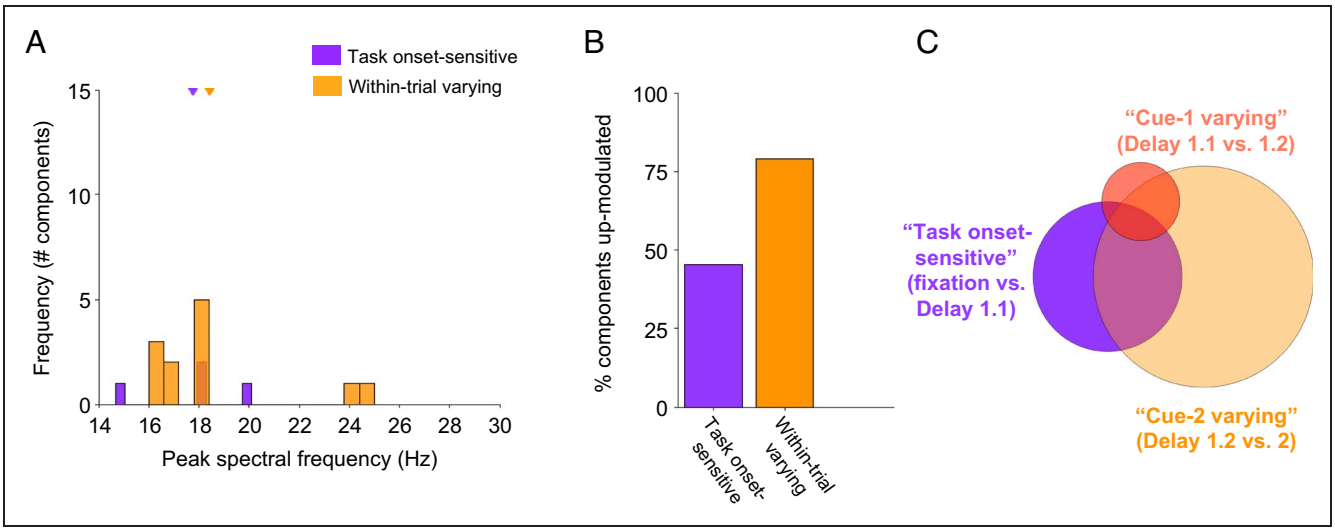

Figure A2. Characteristics of central beta components selected for the primary analyses. (A) Peak spectral frequency (Hz) distribution for the set of 11 task onset-sensitive components (purple) and for the set of 19 non-overlapping within-trial varying components (orange). The triangles denote the mean peak frequency for the two groups = 17.8 Hz and 18.4 Hz, respectively. (B) Percentage of components up-modulated for the two sets of components, with increases reflecting greater loading during Delay 1.1 after the sample in comparison to fixation for task onset-sensitive components and increases reflecting greater loading during early Delay 1.2 compared with late Delay 1.1 and early Delay 2 compared with late Delay 1.2 for within-trial varying components. (C) Distribution of overlap among the three component types. Note that nine components did not survive any of the thresholding procedures.

Table A2. Breakdown of Central Beta Components

	Central Beta Component Classification				
	Task Onset-sensitive	*Within-trial Varying*	*Cue 1-Varying*	*Cue 2-Varying*	*Residual*
Total classified	11	25(w/ overlap); 19 (w/o overlap)	3; 1	24; 18	9
Participant contributions	0–2 $M = 0.92$	0–5 $M = 1.6$ (w/o overlap)	0–1 $M = 0.1$ (w/o overlap)	0–5 $M = 1.4$ (w/o overlap)	0–2 $M = 0.75$

which had an average peak frequency of 17.8 Hz (SD = 2.1 Hz). Five task onset-sensitive central beta components exhibited an increase in loading (45.5%), and six exhibited a decrease in loading.

Three within-trial varying components were identified by contrasting trial loadings between Delay 1.1 and Delay 1.2 ("Cue 1-varying"), and 24 task-insensitive components were identified by contrasting trial loadings between Delay 1.2 and Delay 2 ("Cue 2-varying"). Like the posterior beta and posterior alpha components, the three sets of central beta components overlapped considerably—the 19 components that were identified only in the within-trial contrasts related to the cues were included as the within-trial varying component set.

The average peak frequency of the within-trial varying components was 18.4 Hz (SD = 2.97 Hz), which did not differ in frequency relative to that of the task onset-sensitive central beta components, $t(14) = 0.4126$, $p = .67$. Fourteen within-trial varying components had an increase in loading (78.6%), and five had a decrease, a relative proportion that did not vary from the task onset-sensitive central beta components, $\chi^2(1) = 1.671, p = .196$.

Nine of the central beta components were not identified by any of these contrasts and were excluded from further analysis. For the final set to be analyzed, each participant contributed zero to five components with a mode contribution of two. The resulting set of central beta components were analyzed using the primary statistical analyses of interest to serve as a basis for comparison/control in interpretation of the results from the posterior beta components.

Dynamics of Low-frequency Component Loadings across Delay Periods, and Their Sensitivity to spTMS—Up- versus Down-modulated Components

We addressed whether the nature of posterior beta modulation (i.e., up- vs. down-modulation) observed in our preselection contrasts resulted in different dynamics across delay periods and sensitivity to spTMS (Figure A3).

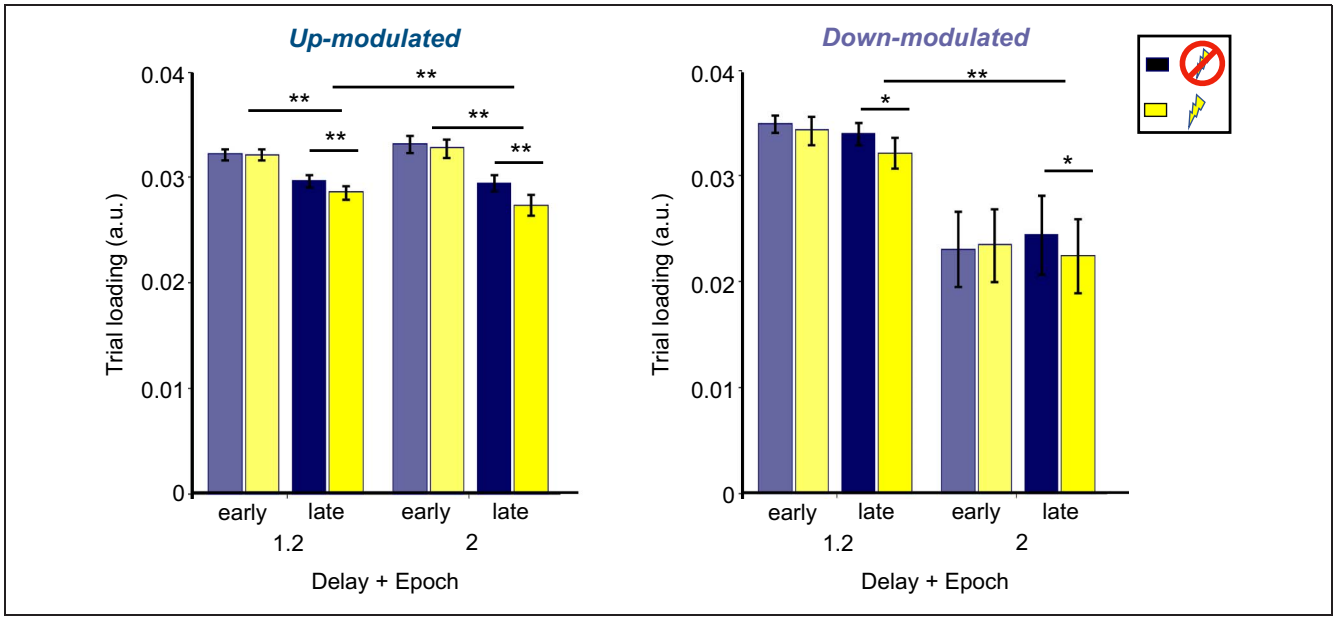

Figure A3. Component loadings as a function of trial epoch and spTMS delivery. Left: For up-modulated posterior beta components, loadings decline across both delay periods when spTMS is absent, an effect that is exaggerated when spTMS is present. Late-delay period epoch loadings are also smaller during Delay 2 than Delay 1.2. Right: Down-modulated posterior beta components decline from Delay 1.2 to Delay 2 and exhibit spTMS sensitivity. Error bars correspond to ± 1 *SEM* across the number of components; *$p < .05$; **$p < .01$.

The majority of components were up-modulated. For these components, a linear mixed-effects model first revealed a significant main effect of delay period epoch, that is, early versus late; $F(1, 253) = 66.238$, $p < .001$, whereby loadings declined from the early to late-delay period epochs ($p < .001$ for both delays). A second linear mixed-effects model revealed a significant main effect of spTMS, $F(1, 253) = 13.516$, $p < .001$, on late-delay period epoch loadings. Specifically, spTMS had the effect of reducing trial loadings, that is, the reductions in loading from early to late-delay period epochs were greater when spTMS was delivered ($p \leq .002$ for comparisons in both delay periods). The linear mixed-effects model did not reveal a main effect of delay period, $F(1, 253) = 2.5546$, $p = .111$, meaning that late-delay period loadings were not different during Delay 1.2 versus Delay 2.

For the down-modulated posterior beta components, the delay period-related component loading dynamics differed in comparison to the up-modulated components. A linear mixed-effects model first revealed no effect of delay period epoch, that is, early versus late; $F(1, 53) = .0905$, $p = .765$, with no change in loadings from the early- to late-delay period epochs ($p \geq .133$ for both delays). A second linear mixed-effects model also did not reveal a significant main effect of spTMS, $F(1, 53) = .7364$, $p = .395$, on late-delay period epoch loadings. However, visual inspection of the late-delay period epoch loadings with and without TMS revealed a qualitative pattern like that observed for up-modulated components, whereby TMS is associated with a larger reduction in trial loading compared with when TMS was not delivered. A post hoc statistical analysis of these late-delay period differences on trial loading with and without TMS delivery indicated that the reduction was significant after the TMS pulses ($p \leq .0467$ for both comparisons). Finally, the linear mixed-effects model revealed a significant main effect of delay period, $F(1, 53) = 18.116$, $p < .001$, whereby late-delay period loadings decreased from Delay 1.2 to Delay 2.

Corresponding author: Jacqueline M. Fulvio, 1202 West Johnson St., Madison, WI 53706–1611, or via e-mail: jacqueline.fulvio@wisc.edu.

Data Availability Statement

Researchers may email the corresponding author to request materials.

Author Contributions

Jacqueline M. Fulvio: Conceptualization; Data curation; Formal analysis; Investigation; Methodology; Project administration; Software; Visualization; Writing—Original draft; Writing—Review & editing. Saskia Haegens: Conceptualization; Formal analysis; Methodology; Software; Writing—Review & editing. Bradley R. Postle: Conceptualization; Funding acquisition; Methodology; Project administration; Resources; Supervision; Writing—Review & editing.

Funding Information

National Institute of Mental Health (https://dx.doi.org/10.13039/100000025), grant number: 2R01MH095984-06.

Diversity in Citation Practices

Retrospective analysis of the citations in every article published in this journal from 2010 to 2021 reveals a persistent pattern of gender imbalance: Although the proportions of authorship teams (categorized by estimated gender identification of first author/last author) publishing in the *Journal of Cognitive Neuroscience* (*JoCN*) during this period were M(an)/M = .407, W(oman)/M = .32, M/W = .115, and W/W = .159, the comparable proportions for the articles that these authorship teams cited were M/M = .549, W/M = .257, M/W = .109, and W/W = .085 (Postle and Fulvio, *JoCN*, 34:1, pp. 1–3). Consequently, *JoCN* encourages all authors to consider gender balance explicitly when selecting which articles to cite and gives them the opportunity to report their article's gender citation balance. The authors of this paper report its proportions of citations by gender category to be: M/M = .676; W/M = .216; M/W = .081; W/W = .027.

Notes

1. Although we have previously referred to the phenomenon as "UMI reactivation," this formulation risks conflation of the psychological construct of reactivating a mental representation and the physiological phenomenon of increasing the level of activity in a circuit. Consequently, when intending the psychological meaning, we will use "involuntary retrieval."
2. The initially uncued item can later return to decodability during the second half of the trial, if cued by the second retrocue (LaRocque, Lewis-Peacock, Drysdale, Oberauer, & Postle, 2013).
3. Note that this data set was not originally collected with the plan to apply the SPACE decomposition, but rather to replicate and extend the results from Rose and colleagues (2016), with similar methods. To our knowledge, this is the first application of the SPACE decomposition to EEG data (previous publications have featured magnetoencephalography (van der Meij et al., 2015; 2016), and so we lacked an empirical basis from which to estimate a priori the sample size that might be needed to meaningfully relate variation in SPACE components of EEG signals to behavior.
4. We note that when these analyses were initially carried out separately for the two categories of posterior beta components, for task onset-sensitive components, the linear mixed-effects model applied to the former identified a significant negative relationship between the early-to-late decrease in component loading and behavioral accuracy, $F(1, 90) = 4.8522$, $p = .03$, no delay period by TMS delivery interaction, $F(1, 90) = 0.0411$, $p = .84$, and when broken out by spTMS condition the relationship was significant for spTMS-present, $F(1, 44) = 11.973$, $p = .001$, but absent for spTMS-absent, $F(1, 45) = 0.0209$, $p = .89$. For within-trial varying components, in contrast, these analyses yielded no significant effects.

REFERENCES

Axmacher, N., Schmitz, D. P., Wagner, T., Elger, C. E., & Fell, J. (2008). Interactions between medial temporal lobe, prefrontal cortex, and inferior temporal regions during visual working memory: A combined intracranial EEG and functional magnetic resonance imaging study. *Journal of Neuroscience*, *28*, 7304–7312. https://doi.org/10.1523/JNEUROSCI.1778-08.2008, PubMed: 18632934

Baker, S. N. (2007). Oscillatory interactions between sensorimotor cortex and the periphery. *Current Opinion in Neurobiology*, *17*, 649–655. https://doi.org/10.1016/j.conb.2008.01.007, PubMed: 18339546

Barak, O., & Tsodyks, M. (2014). Working models of working memory. *Current Opinion in Neurobiology*, *25*, 20–24. https://doi.org/10.1016/j.conb.2013.10.008, PubMed: 24709596

Bastos, A. M., Usrey, W. M., Adams, R. A., Mangun, G. R., Fries, P., & Friston, K. J. (2012). Canonical microcircuits for predictive coding. *Neuron*, *76*, 695–711. https://doi.org/10.1016/j.neuron.2012.10.038, PubMed: 23177956

Bastos, A. M., Vezoli, J., Bosman, C. A., Schoffelen, J.-M., Oostenveld, R., Dowdall, J. R., et al. (2015). Visual areas exert feedforward and feedback influences through distinct frequency channels. *Neuron*, *85*, 390–401. https://doi.org/10.1016/j.neuron.2014.12.018, PubMed: 25556836

Bastos, A. M., Loonis, R., Kornblith, S., Lundqvist, M., & Miller, E. K. (2018). Laminar recordings in frontal cortex suggest distinct layers for maintenance and control of working memory. *Proceedings of the National Academy of Sciences, U.S.A.*, *115*, 1117–1122. https://doi.org/10.1073/pnas.1710323115, PubMed: 29339471

Buschman, T. J., Denovellis, E. L., Diogo, C., Bullock, D., & Miller, E. K. (2012). Synchronous oscillatory neural ensembles for rules in the prefrontal cortex. *Neuron*, *76*, 838–846. https://doi.org/10.1016/j.neuron.2012.09.029, PubMed: 23177967

de Hemptinne, C., Ryapolova-Webb, E. S., Air, E. L., Garcia, P. A., Miller, K. J., Ojemann, J. G., et al. (2013). Exaggerated phase-amplitude coupling in the primary motor cortex in Parkinson disease. *Proceedings of the National Academy of Sciences, U.S.A.*, *110*, 4780–4785. https://doi.org/10.1073/pnas.1214546110, PubMed: 23471992

Deiber, M.-P., Missonnier, P., Bertrand, O., Gold, G., Fazio-Costa, L., Ibañez, V., et al. (2007). Distinction between perceptual and attentional processing in working memory tasks: A study of phase-locked and induced oscillatory brain dynamics. *Journal of Cognitive Neuroscience*, *19*, 158–172. https://doi.org/10.1162/jocn.2007.19.1.158, PubMed: 17214572

Delorme, A., & Makeig, S. (2004). EEGLAB: An open source toolbox for analysis of single-trial EEG dynamics including independent component analysis. *Journal of Neuroscience Methods*, *134*, 9–21. https://doi.org/10.1016/j.jneumeth.2003.10.009, PubMed: 15102499

ElShafei, H. A., Zhou, Y. J., & Haegens, S. (2022). Shaping information processing: The role of oscillatory dynamics in a working memory task. *eNeuro*, *9*, ENEURO.0489-21.2022. https://doi.org/10.1523/ENEURO.0489-21.2022, PubMed: 35977824

Engel, A. K., & Fries, P. (2010). Beta-band oscillations—Signalling the status quo? *Current Opinion in Neurobiology*, *20*, 156–165. https://doi.org/10.1016/j.conb.2010.02.015, PubMed: 20359884

Fulvio, J. M., & Postle, B. R. (2020). Cognitive control, not time, determines the status of items in working memory. *Journal of Cognition*, *3*, 8. https://doi.org/10.5334/joc.98, PubMed: 32292872

Haegens, S., Vergara, J., Rossi-Pool, R., Lemus, L., & Romo, R. (2017). Beta oscillations reflect supramodal information during perceptual judgment. *Proceedings of the National Academy of Sciences, U.S.A.*, *114*, 13810–13815. https://doi.org/10.1073/pnas.1714633115, PubMed: 29229820

Kilavik, B. E., Confais, J., Ponce-Alvarez, A., Diesmann, M., & Riehle, A. (2010). Evoked potentials in motor cortical local field potentials reflect task timing and behavioral performance. *Journal of Neurophysiology*, *104*, 2338–2351. https://doi.org/10.1152/jn.00250.2010, PubMed: 20884766

Kornblith, S., Buschman, T. J., & Miller, E. K. (2016). Stimulus load and oscillatory activity in higher cortex. *Cerebral Cortex*, *26*, 3772–3784. https://doi.org/10.1093/cercor/bhv182, PubMed: 26286916

Kundu, B., Chang, J.-Y., Postle, B. R., & Van Veen, B. D. (2015). Context-specific differences in fronto-parieto-occipital effective connectivity during short-term memory maintenance. *Neuroimage*, *114*, 320–327. https://doi.org/10.1016/j.neuroimage.2015.04.001, PubMed: 25863155

LaRocque, J. J., Lewis-Peacock, J. A., Drysdale, A. T., Oberauer, K., & Postle, B. R. (2013). Decoding attended information in short-term memory: An EEG study. *Journal of Cognitive Neuroscience*, *25*, 127–142. https://doi.org/10.1162/jocn_a_00305, PubMed: 23198894

Lundqvist, M., Rose, J., Herman, P., Brincat, S. L., Buschman, T. J., & Miller, E. K. (2016). Gamma and beta bursts underlie working memory. *Neuron*, *90*, 152–164. https://doi.org/10.1016/j.neuron.2016.02.028, PubMed: 26996084

McFarland, D. J., Miner, L. A., Vaughan, T. M., & Wolpaw, J. R. (2000). Mu and beta rhythm topographies during motor imagery and actual movements. *Brain Topography*, *12*, 177–186. https://doi.org/10.1023/A:1023437823106, PubMed: 10791681

Miller, E. K., Lundqvist, M., & Bastos, A. M. (2018). Working memory 2.0. *Neuron*, *100*, 463–475. https://doi.org/10.1016/j.neuron.2018.09.023, PubMed: 30359609

Mutanen, T. P., Biabani, M., Sarvas, J., Ilmoniemi, R. J., & Rogasch, N. C. (2020). Source-based artifact-rejection techniques available in TESA, an open-source TMS-EEG toolbox. *Brain Stimulation*, *13*, 1349–1351. https://doi.org/10.1016/j.brs.2020.06.079, PubMed: 32659484

Neuper, C., Wörtz, M., & Pfurtscheller, G. (2006). ERD/ERS patterns reflecting sensorimotor activation and deactivation. In C. Neuper & W. Klimesch (Eds.), *Progress in brain research* (Vol. 159, pp. 211–222). Elsevier. https://doi.org/10.1016/S0079-6123(06)59014-4

Nunez, P. L., & Srinivasan, R. (2006). *Electric fields of the brain: The neurophysics of EEG*. New York: Oxford University Press.

Oostenveld, R., Fries, P., Maris, E., & Schoffelen, J.-M. (2011). FieldTrip: Open source software for advanced analysis of MEG, EEG, and invasive electrophysiological data. *Computational Intelligence and Neuroscience*, *2011*, 156869. https://doi.org/10.1155/2011/156869, PubMed: 21253357

Pereira, J., & Wang, X.-J. (2015). A tradeoff between accuracy and flexibility in a working memory circuit endowed with slow feedback mechanisms. *Cerebral Cortex*, *25*, 3586–3601. https://doi.org/10.1093/cercor/bhu202, PubMed: 25253801

Proskovec, A. L., Wiesman, A. I., Heinrichs-Graham, E., & Wilson, T. W. (2019). Load effects on spatial working memory performance are linked to distributed alpha and beta oscillations. *Human Brain Mapping*, *40*, 3682–3689. https://doi.org/10.1002/hbm.24625, PubMed: 31077487

Rassi, E., Zhang, Y., Mendoza, G., Méndez, J. C., Merchant, H., & Haegens, S. (2023). Distinct beta frequencies reflect

categorical decisions. *Nature Communications*, *14*, 2923. https://doi.org/10.1038/s41467-023-38675-3, PubMed: 37217510

Rogasch, N. C., Sullivan, C., Thomson, R. H., Rose, N. S., Bailey, N. W., Fitzgerald, P. B., et al. (2017). Analysing concurrent transcranial magnetic stimulation and electroencephalographic data: A review and introduction to the open-source TESA software. *Neuroimage*, *147*, 934–951. https://doi.org/10.1016/j.neuroimage.2016.10.031, PubMed: 27771347

Romei, V., Brodbeck, V., Michel, C., Amedi, A., Pascual-Leone, A., & Thut, G. (2008). Spontaneous fluctuations in posterior α-band EEG activity reflect variability in excitability of human visual areas. *Cerebral Cortex*, *18*, 2010–2018. https://doi.org/10.1093/cercor/bhm229, PubMed: 18093905

Rosanova, M., Casali, A., Bellina, V., Resta, F., Mariotti, M., & Massimini, M. (2009). Natural frequencies of human corticothalamic circuits. *Journal of Neuroscience*, *29*, 7679–7685. https://doi.org/10.1523/JNEUROSCI.0445-09.2009, PubMed: 19535579

Rose, N. S., LaRocque, J. J., Riggall, A. C., Gosseries, O., Starrett, M. J., Meyering, E. E., et al. (2016). Reactivation of latent working memories with transcranial magnetic stimulation. *Science*, *354*, 1136–1139. https://doi.org/10.1126/science.aah7011, PubMed: 27934762

Salmelin, R., & Hari, R. (1994). Spatiotemporal characteristics of sensorimotor neuromagnetic rhythms related to thumb movement. *Neuroscience*, *60*, 537–550. https://doi.org/10.1016/0306-4522(94)90263-1, PubMed: 8072694

Samaha, J., Gosseries, O., & Postle, B. R. (2017). Distinct oscillatory frequencies underlie excitability of human occipital and parietal cortex. *Journal of Neuroscience*, *37*, 2824–2833. https://doi.org/10.1523/JNEUROSCI.3413-16.2017, PubMed: 28179556

Siegel, M., Warden, M. R., & Miller, E. K. (2009). Phase-dependent neuronal coding of objects in short-term memory. *Proceedings of the National Academy of Sciences, U.S.A.*, *106*, 21341–21346. https://doi.org/10.1073/pnas.0908193106, PubMed: 19926847

Stokes, M. G. (2015). 'Activity-silent' working memory in prefrontal cortex: A dynamic coding framework. *Trends in Cognitive Sciences*, *19*, 394–405. https://doi.org/10.1016/j.tics.2015.05.004, PubMed: 26051384

Spitzer, B., & Haegens, S. (2017). Beyond the status quo: A role for beta oscillations in endogenous content (re)activation. *eNeuro*, *4*, ENEURO.0170-17.2017. https://doi.org/10.1523/ENEURO.0170-17.2017, PubMed: 28785729

Tallon-Baudry, C., Bertrand, O., Peronnet, F., & Pernier, J. (1998). Induced γ-band activity during the delay of a visual short-term memory task in humans. *Journal of Neuroscience*, *18*, 4244–4254. https://doi.org/10.1523/JNEUROSCI.18-11-04244.1998, PubMed: 9592102

van der Meij, R., Jacobs, J., & Maris, E. (2015). Uncovering phase-coupled oscillatory networks in electrophysiological data. *Human Brain Mapping*, *36*, 2655–2680. https://doi.org/10.1002/hbm.22798, PubMed: 25864927

van Der Meij, R., van Ede, F., & Maris, E. (2016). Rhythmic components in extracranial brain signals reveal multifaceted task modulation of overlapping neuronal activity. *PLoS One*, *11*, e0154881. https://doi.org/10.1371/journal.pone.0154881, PubMed: 27336159

van Wijk, B. C. M., Daffertshofer, A., Roach, N., & Praamstra, P. (2009). A role of beta oscillatory synchrony in biasing response competition? *Cerebral Cortex*, *19*, 1294–1302. https://doi.org/10.1093/cercor/bhn174, PubMed: 18836098

von Lautz, A. H., Herding, J., Ludwig, S., Nierhaus, T., Maess, B., Villringer, A., et al. (2017). Gamma and beta oscillations in human MEG encode the contents of vibrotactile working memory. *Frontiers in Human Neuroscience*, *11*, 576. https://doi.org/10.3389/fnhum.2017.00576, PubMed: 29255408

Walsh, V., & Rushworth, M. (1999). A primer of magnetic stimulation as a tool for neuropsychology. *Neuropsychologia*, *37*, 125–135. PubMed: 10080370

Wan, Q., Ardalan, A., Fulvio, J. M., & Postle, B. R. (2024). Representing context and priority in working memory. *Journal of Cognitive Neuroscience*, *36*, 1374–1394. https://doi.org/10.1162/jocn_a_02166, PubMed: 38683726

Wan, Q., Cai, Y., Samaha, J., & Postle, B. R. (2020). Tracking stimulus representation across a 2-back visual working memory task. *Royal Society Open Science*, *7*, 190228. https://doi.org/10.1098/rsos.190228, PubMed: 32968489

Wan, Q., Menendez, J. A., & Postle, B. R. (2022). Priority-based transformations of stimulus representation in visual working memory. *PLoS Computational Biology*, *18*, e1009062. https://doi.org/10.1371/journal.pcbi.1009062, PubMed: 35653404

Wessel, J. R., & Anderson, M. C. (2024). Neural mechanisms of domain-general inhibitory control. *Trends in Cognitive Sciences*, *28*, 124–143. https://doi.org/10.1016/j.tics.2023.09.008

Yu, Q., Teng, C., & Postle, B. R. (2020). Different states of priority recruit different neural representations in visual working memory. *PLoS Biology*, *18*, e3000769. https://doi.org/10.1371/journal.pbio.3000769, PubMed: 32598358